POLITECNICO DI TORINO

Master's Degree in Biomedical Engineering

Master's Degree Thesis

"Optical coherence tomography angiography and automatic vascular analysis: seeing skin lesions from a different perspective"

Supervisors

Prof. Kristen MEIBURGER

Prof. Filippo MOLINARI

Dr. Mengyang LIU

Candidate

Giulia ROTUNNO

Academic year 2020/2021

Summary

The types of skin lesions are innumerable: from a mere wound, to an uncomfortable seborrheic keratosis, up to a severe basal cell carcinoma. Many dermatologic studies have been done with different imaging approaches, some of which explore not the structural aspect of the lesion but its blood flow, proving that the vasculature plays a fundamental role in the distinction between healthy skin and diseased skin. The goal of this thesis work, done in collaboration with the Medical University of Vienna, is to analyze the vascular network of skin lesions in a completely non-invasive and automatic way. The lesions observed in the laboratory and presented here are seborrheic keratosis, wounds and cherry angiomas.

The non-invasiveness is achieved thanks to an imaging technique called *optical coherence tomography angiography* that has given promising results in recent years. This technique enables a volumetric rendering of the vascular network of the target sample without the need of any contrast agent. Moreover, since a laser beam is employed for the investigation of the skin, the radiations adopted are non-ionizing. Skeletonization and parameter extraction in different regions of interest are, instead, the key steps for the automatic lesion area determination. After an overview of the imaging technique principles, this thesis exposes the complete study carried out: how the patient imaging sessions took place, how the raw data were processed, the explanation of the parameter extraction procedure and the final segmentation of the lesion area. A particular focus is made on the methods adopted for the attenuation of the artifacts that mainly affect optical coherence tomography angiography tomograms: projection artifact and motion artifact.

This thesis work shows how beneficial the fascinating collaboration between medicine and engineering could be. In fact, the study presented here shows how it is possible to obtain quantitative results that can allow, among others:

- the monitoring of wound healing,
- a more accurate surgical removal of seborrheic keratosis,
- a proper follow-up care after treatment of basal cell carcinoma.

Acknowledgements

My supervisor prof. Meiburger for offering me a fascinating thesis topic and for giving me the opportunity to conclude my studies with an experience abroad.

The Center for Medical Physics and Biomedical Engineering at the Medical University of Vienna, expecially Dr. Mengyang, Lisa Krainz and Sam Mathew, for welcoming me warmly in their lab and for teaching me the 'darkest secrets' of OCT.

My two fellow travellers, the 'best carbonara man' Simone and the 'araldica lover' Max, for the wonderful company during these months in Vienna.

My student dorm mates in Vienna, especially Clemens and Charlotte, for making me spend amazing moments even during a pandemic lockdown.

My university colleagues, for all the joy and anxiety shared together in those years and for the most intense nightly chats on plastic chairs.

My lifetime friends, for supporting me whenever I needed.

And last but not least my crazy family, the most beautiful thing that I have.

Table of Contents

List of Figures

Chapter 1

Optical coherence tomography

Optical coherence tomography (OCT) is an optical tomographic technique that has achieved quite a success in the medical field, first of all in ophtalmology. Recently other medical specialties, such as dermatology, employ OCT techniques as a diagnostic tool obtaining excellent results. In this chapter I will analyze how OCT works, its advantages and its limitations.

1.1 OCT main principles

First of all let's decompose the name *Optical coherence tomography*.

- **Optical**
  OCT is an optical imaging procedure: light is the fundamental element. Light is an electromagnetic wave and the electric and magnetic fields oscillate in time and space. Each light beam used is characterized by an amplitude and a wavelength.
- **Coherence**
  In physics, coherence is a property of light. Two waves are perfectly coherent if their frequencies and waveforms are identical and if their phase difference is constant. Only monochromatic light can be perfectly coherent.
- **Tomography**
  The OCT methodology allows to obtain 1D scans of the sample. Through raster-scanning we can recreate the 3D tissue volume under study.

We shall add a fourth essential word in order to explain OCT: **interference**. This is a phenomenon that occurs when two or more electromagnetic waves interact

with each other. The result of the interference is the sum of the waves involved. There are two extreme cases that can happen: if the waves are *in phase* they interfere constructively, whereas if the waves are 180° *out of phase* the interference is destructive.

OCT basically measures the reflectivity of the tissue as a function of depth thanks to the interference phenomena of a low coherence light source. It is based on the idea of the Michelson interferometer that I will briefly introduce.

1.1.1 Michelson interferometer

The Michelson interferometer is composed of the following components: a light source, a reference mirror, a beam spitter, a sample and a photodetector. We can see a basic scheme of a Michelson interferometer in Fig. 1.1; in this case the sample is a human eye.

The working principle consists in the projection of a light beam, then split into two beams (sample beam and reference beam) by a beam splitter. The sample beam hits the target that we want to investigate and the reference beam hits a reference mirror at a known distance. The reflected beams travel the same paths in reverse until they reach again the beam splitter: here they recombine and the resulting interference is acquired by the detector. Basically the echo time delay of the light reflected by the target and caught by the detector is compared with the echo time delay of the light reflected by the reference mirror and caught by the same detector. A maximum interference is produced when the light reflected by the sample and the reference mirror arrive simultaneously. The interferometer integrates several data points collected in depth and laterally until it reconstructs a tomogram of the target sample.

If a monochromatic beam is used, perfect coherence is obtained. In this case a constructive interference takes place whenever the two detected waves (the reference beam and the sample beam) are *in phase*. This happens when the pathlength of the reference beam and the pathlength of the sample beam are equal or one is shifted in respect to the other of a multiple of the wave's period.

Since it is useful to know exactly at which depth in the sample a certain reflective surface is, it would be dutiful that we notice a constructive interference only when the pathlength of the reference arm is equal to the pathlength of the sample arm. As we stated, this is not the case and as a consequence we will notice never be able to locate the reflective surface of the sample. This is why in OCT a perfect coherent light source would be useless; we will instead talk about low coherence

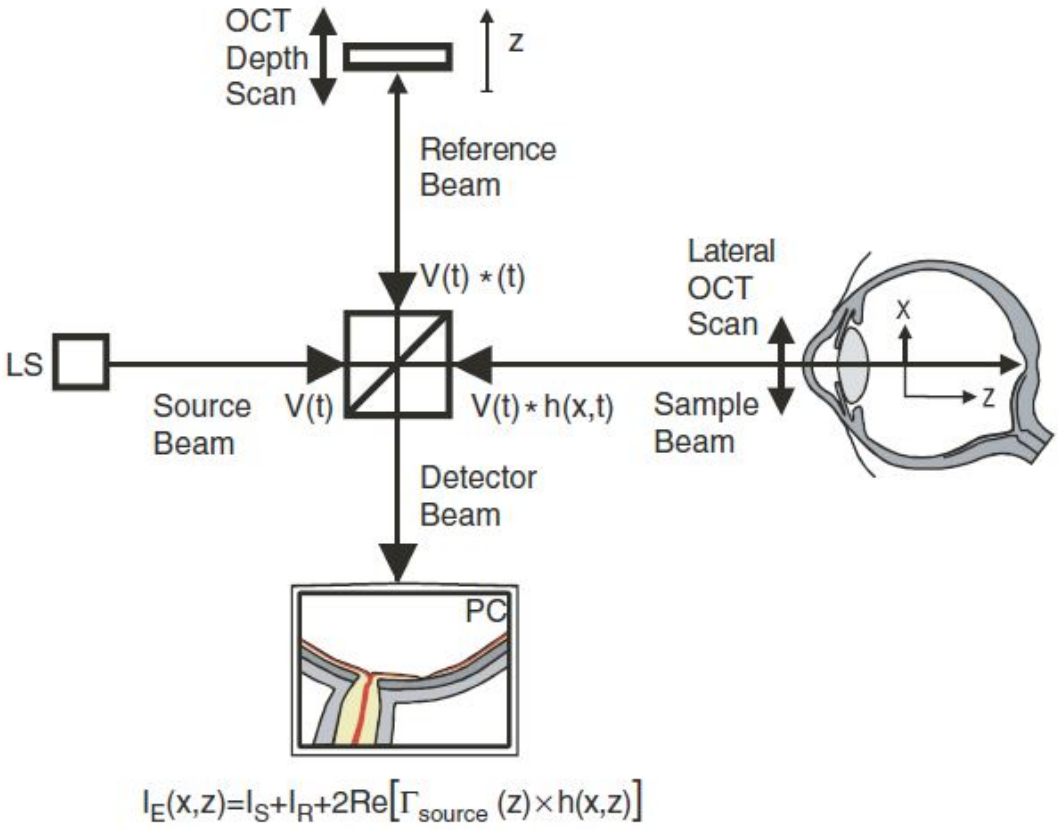

Figure 1.1: OCT scheme based on a low time-coherence Michelson interferometer. [1] V(t) is the analytic signal, h(x,t) is the sample response, $I_E(x,z)$ is the total intensity at the interferometer exit.

light sources.

1.1.2 Low coherence interference

In order to have a refractive depth profile, a low coherent light source is used, usually a broadband Gaussian source, where the amplitude and the phase difference between the waves remain constant for a brief time (coherence time) and for a short length (coherence length).

The **coherence length** is [1]:

$$l_c = \frac{2ln2}{\pi}\frac{\lambda_0^2}{\Delta\lambda} \tag{1.1}$$

where, assuming a Gaussian shape of the spectrum of the emitted light, λ_0 is its central wavelength and $\Delta\lambda$ its spectral width.

The coherence length is proportional to the wavelength of light squared over the bandwidth. With a small bandwidth (perfect coherence) the interference signal have a lot of maxima; with a wider bandwidth the light is less coherent and the interference signal has only one maximum when the pathlength of the reference beam is equal to the pathlength of the sample beam within the so called **coherence volume**. The less is the coherence, the smaller is the coherence volume, the higher is the resolution with which we can locate the reflective surface in the sample.

There are different ways to get depth information. In Time-domain OCT for example, we have to scan the reference mirror and record the intensity profiles detected, corresponding to the reflective profiles of the sample. We will see in the next section that there are other OCT techniques which don't need any movement of mechanical parts.

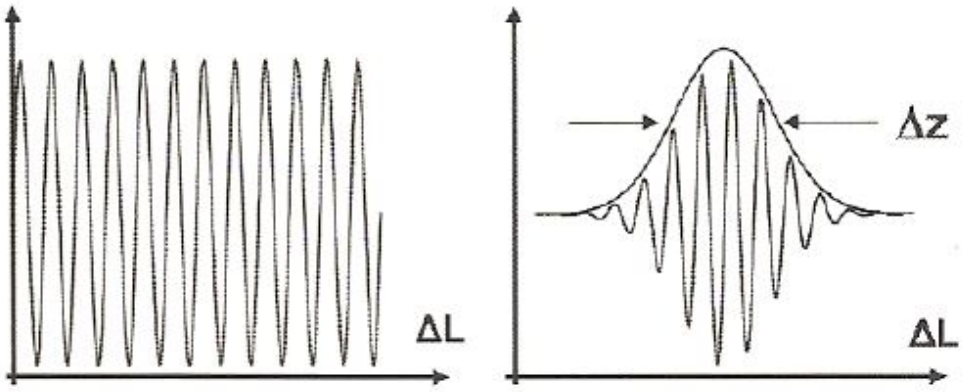

Figure 1.2: Representation of a perfectly coherent light (on the left) and a low coherent light (on the right). Δz is the coherence length.

1.2 OCT techniques

At the exit of a standard interferometer a detector, generally a photodetector, provides a measure of the resulting signal as a current. The averaged intensity at the interferometer exit is the **interference signal** and can be decomposed in [1]:

$$\langle I_E(t;\Delta t)\rangle = \langle I_S(t)\rangle + \langle I_R(t)\rangle + G_{SR}(\Delta t). \tag{1.2}$$

$I_R(t)$ is the intensity of the beam arriving at the detector after hitting the reference mirror, $I_S(t)$ is the intensity of the beam arriving at the detector if there would

be just the scattering object and not the reference mirror and $G_{SR}(\Delta t)$ is the interference term or cross-correlation term.

We are particularly interested in the **interference term**, that is twice the real part of the cross-correlation of the analytic signals of the two interfering beams ($V_S(t)$ and $V_R(t)$) [1]:

$$G_{SR}(\Delta t) = 2Re\langle V_S^*(t)V_R(t+\Delta t)\rangle = 2Re\Gamma_{SR}(\Delta t). \tag{1.3}$$

Δt is the delay between the time that the light takes to go from the movable mirror to the detector and the time that it takes to go from the scattering object to the detector. When Δt=0 the interference is completely constructive and maximum.

The cross-correlation function can be expressed as follows [1]:

$$\Gamma_{SR}(\Delta t) = (1/2)G(\Delta t) + (i/2)HT(G(\Delta t)), \tag{1.4}$$

where HT stands for Hilbert transform.

It is useful to switch to the **spectral domain**. Since the Fourier transform of the auto-correlation of a light wave is its power spectrum, the cross-spectral density function of the two waves that we are considering in this paragraph is [1]:

$$W_{SR}(\upsilon) = FT(\Gamma_{SR}(\Delta t)), \tag{1.5}$$

where υ is the optical frequency (seconds per cycle), related to omega (angular frequency).

The corresponding spectral domain of the Eq. 1.2 is [1]:

$$S(\upsilon;\Delta t) = S_S(\upsilon) + S_R(\upsilon) + 2Re[W_{SR}(\upsilon)]cos(2\pi\upsilon\Delta t) \tag{1.6}$$

and it is the mathematical expression of the so called spectral interference law.

There are three principal OCT techniques that differ from each other in the way of scanning the sample.

1.2.1 Time domain OCT

In a Time domain OCT system (**TD-OCT**) the reference mirror is moved between a minimum and a maximum position in order to acquire all the echos from each depth of the target tissue; considering that we are using a low coherence light beam, interference is obtained only if the distance traveled by the backscattered beam in the sample arm is the same traveled by the backscattered beam in the reference arm. The sample information is included in the inteference term of the signal detected by the photodetector. The TD-OCT is based on the convolution operation presented in Eq. 1.3.

It's worth recalling that since we are using a low-coherent light source and assuming that the scanning direction of the sample is the z direction, the interference term gives intensity information about the sample within Δz, where Δz is the width of the coherence function of the source. The depth resolution is correlated to Δz too.

The main disadvantage of this technique is that two types of scanning has to be performed to get a 2D or 3D image, the depth scan by moving the mirror and the lateral scan by moving the light beam. This results to be time consuming.

1.2.2 Spectral domain OCT

To solve the main issue of TD-OCT, a series of Fourier domain OCT (FD-OCT) techniques were developed, such as Spectral domain OCT (**SD-OCT**) and Swept source OCT (SS-OCT). With FD-OCT depth scan information can be obtained without moving the mirror.

At the exit of a SD-OCT system a spectrometer takes the place of the photodetector. The spectrometer consists of a grating that separates the different wavelengths of the detected light and of a linear array of light-sensitive elements (CCD or CMOS); as soon as they are invested by the recombinant beam, they are able to detect interference of the light signal based on its wavelengths.

The spectrometric measurement gives the information of the spectrum of the backscattered light. By making a Fourier transform of the field amplitude of the sample beam $A_S(K)$, we can obtain the scattering potential $F_S(z)$ of the scanning line as a function of depth. The spectral intensity at the interferometer exit is [1]:

$$I_{SR}(K) = I_S(K) + I_R(K) + 2\sqrt{I_S(K)I_R(K)}Re\{\mu(K)e^{i[\Phi_S(K)-\Phi_R(K)]}\}. \quad (1.7)$$

where $I_S(K) = |A_S(K)|^2$ is the spectral intensity (or power spectrum) of the sample beam, and $A_S(K) = a_S(K)e^{i\Phi_S(K)}$ its complex amplitude. $I_R(K)$ is the power spectrum of the reference beam, and $\mu(K)$ the spectral degree of coherence (=1, in case of monochromatic light). $\Phi_S(K)$ is the spectral phase of the sample wave and $\Phi_R(K)$ the spectral phase of the reference beam [1].

In order to obtain a depth-scan a Fourier operation needs to be done. The relation is the following:

$$F_S(z) \propto FT\{A_S(K)\} \quad (1.8)$$

As we can see the FFT operation assumes that the spectrum samples are in k-space. Therefore, before that operation a re-sampling is usually needed.

The main advantage of SD-OCT is for sure an higher speed of scanning, because no mirror moving is required to gain depth information. The risk of image distortion due to motion in the sample is therefore minimized. Moreover SD-OCT systems offer a fundamental sensitivity advantage over TD-OCT systems [2]. On the other hand SD-OCT systems suffer from a higher financial cost due to the presence of the spectrometer and from an high roll-off, a loss of intensity with distance from the zero delay.

1.2.3 Swept source OCT

Nowadays, the SD-OCT is often replaced by an even faster OCT technique: Swept source OCT (**SS-OCT**). Moreover, swept sources enable spectral resolution in SS-OCT, which can be much higher than that of SD-OCT. Finally the high roll-off that affects SD systems is here solved. The operations are the same as in SD-OCT but two main differences can be highlighted as follows:

- there is a single photodetector or a dual balanced detector (DBD) at the inteferometer exit instead of a spectrometer.
- a frequency swept laser is used as the light source. It emits a single wavelength at a time, covering a wide range of wavelegnths in total.

The SS-OCT systems are widely used in dermatological applications. This is also the type of system that I used for my thesis work.

1.3 OCT signal and system properties

A certain OCT signal originates thanks to discontinuities of the attenuation coefficient or of the refractive index of the target tissue. Both tissue and system characteristics can influence the OCT signal quality. Let's see the most important ones.

Probing depth

OCT imaging is based on light backscattering. Of course not every backscattered photon is ballistic. There are also **multiple scattered photons** and those don't contribute to the image creation but they contribute to the noise background (that leads to less imaging contrast and a worst image resolution). In order to limit the multiple scattered photons detection, we can work on the **probing depth**, that is the distance in the z direction at which multiple scattered photons starts to dominate.

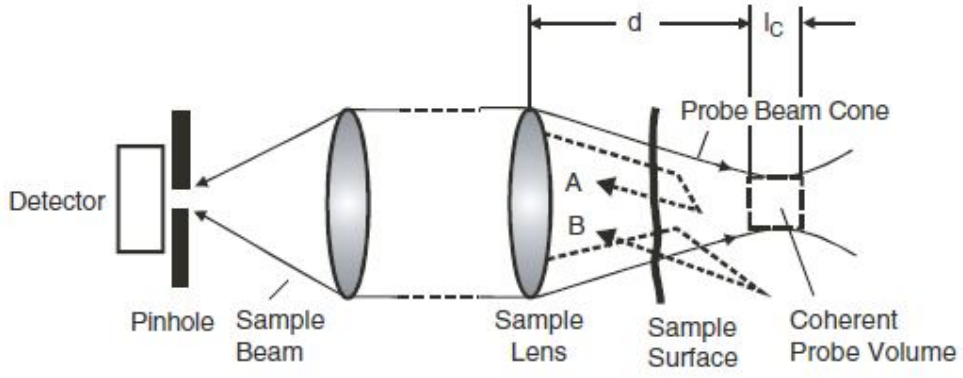

Figure 1.3: Geometry of sample and probing beam [1].

As we can see in the Fig. 1.3 the larger the probing depth d, the fewer scattered photons are avaiable. The photons which trajectories are outside the coherence gate (case A) or which trajectories miss the photodetector (case B) don't contribute to the interferogram.

The probing depth depends principally on the numerical aperture of the imaging optic, NA. With an higher NA the photodector is able to detect more multiple scattered photons. In OCT it is important to find a compromise in order to maintain a good lateral resolution (high NA) and a reasonable depth of focus (low NA).

Sensitivity and SNR

Sensitivity is the ratio between the signal power obtained by the stronger sample reflectivity (an ideally perfectly reflective mirror) and the signal power received from the weakest scattering sample (equal to the noise of the system). The sensitivity is proportional:

- directly to the source power,
- inversely to the electronics bandwidth.

In other words the sensitivity is the minimum value of the input reflectivity signal necessary to produce a specified output interference signal with an SNR equal to 1. The **signal-to-noise ratio** (SNR) is:

$$SNR = 10log\Big(\frac{P_{signal}}{P_{noise}}\Big), \tag{1.9}$$

where P_{signal} is the power of the signal, whereas the power of the noise, P_{noise}, can be represented mathematically by the standard deviation between the data values. The SNR is proportional:

- directly to the signal power and to the photodetector efficiency,
- inversely to the noise power.

The goal is to maximize the sensitivity and the SNR by reducing the noise of the system and by increasing the power of the source, bearing in mind the limitation of the maximum power to which the patient can be expose. Noise can be caused by high source power, electronics, tissue reflectivity, etc.

Resolution

Depth or **axial resolution** depends on the bandwidth of the light source or, we can equally say, on its coherence length. The bandwidth of the source is usually defined by the full width half maximum (FWHM) of the source intensity spectrum.

$$\Delta z = l_c = l_{FWHM}/2 = \frac{2ln2}{\pi}\frac{\lambda_0^2}{\Delta\lambda} \tag{1.10}$$

A further phenomenon that deteriorates the axial resolution is that of **dispersion**. A dispersive medium of path length z adds a frequency-dependent phase to the sample wave [1]:

$$\Phi_{Disp}(\omega) = k(\overline{\omega})z + k^{(1)}(\overline{\omega})(\omega - \overline{\omega})z + k^{(2)}(\overline{\omega})\frac{(\omega - \overline{\omega})^2}{2}z, \tag{1.11}$$

where ω is the frequency, $\overline{\omega}$ is the central frequency of the source beam and $k^{(1)}(\overline{\omega}) = (d^j(k)/d^j(\omega))$ is the j-th order dispersion. In order to compensate this dispersion and correct the phase shift a digital technique is usually used but until the term $(\omega - \overline{\omega})$, namely the bandwidth, is small, the phase shift correction can be left out.

Lateral or **transversal resolution** is defined by the numerical aperture of the objective lens and doesn't depend on the bandwidth of the source. Following Abbe's criteria we can denote the lateral resolution as [3]:

$$\Delta x = 0.61\lambda_0/NA \tag{1.12}$$

Moreover Δx and depth of focus are correlated: a high NA increase the transversal resolution, but at the same time it narrows the depth of focus. Another way to reduce the sidelobes and, as a consequence, to keep a good transversal resolution is to perform a focus tracking over the depth scan.

Penetration depth

This is a parameter strongly affected by the tissue properties, such as absorption coefficient and refractive index. Scattering and absorption are dominant in the range of the near infrared of light spectrum around 800 nm and 1800 nm. By increasing the central wavelength of the source, both absorption and scattering phenomena of the sample decrease. Having an higher wavelength induces an higher penetration depth but on the other hand allows a bigger axial resolution.

For OCT the **wavelength range** used is 600-1550 nm, but for dermatologic applications a central wavelength of 1300 nm is preferred in order to have a good compromise between penetration depth and axial resolution.

Light sources

The most commonly used light sources for OCT are SLD (Superluminescent Diode), LED(Light Emitting Diode), **akinetic swept sources**, ... The properties that a light sources should have are:

- low temporal and spatial coherence properties in order to have a better resolution,
- a reasonable power emission,
- a proper wavelength and bandwidth and
- a point of spread function (PSF) with a narrow half-width and no satellite.

1.4 Laboratory OCT system

In this section I will present the SS-OCT system located at the Center for Medical Physics and Biomedical Engineering at the Medical University of Vienna. This system was used for all the acquisition useful for this thesis work.

First of all here are the main **components**: a laser source, a reference arm, a sample arm, a beam splitter, a dual-balance-detector and a PC workstation. The Fig. 1.4 represents a scheme of the OCT system, whereas Fig. 1.5 and 1.6 are pictures of the reference and sample arm respectively.

The **laser source** (blue square in Fig. 1.7) is a swept source (SS-OCT-1310, Insight Photonic Solutions, Inc, U.S.). As we already discussed previously the swept source allows a faster scan and a higher sensitivity of the system in respect to a normal broadband light source. The central wavelength used for our purpose

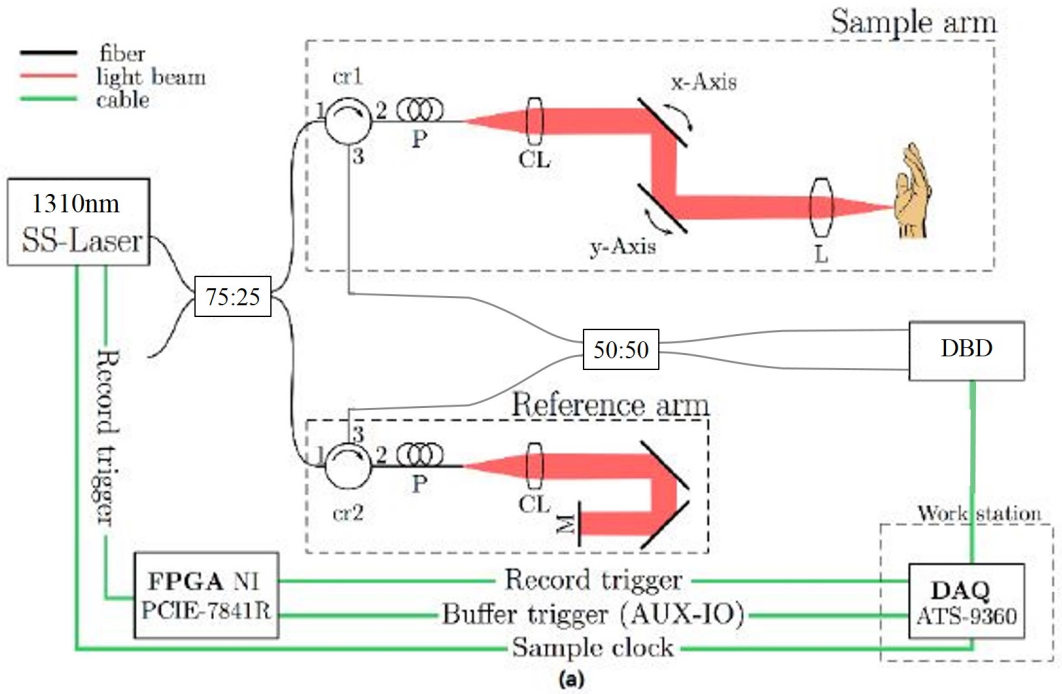

Figure 1.4: Schematic representation of the imaging setup used in the experiments [adapted from [4]].

is 1310 nm and the bandwidth is 29 nm. The swept frequency is 222.22 kHz and the power emitted by the laser is 70 mW. Of course during the path covered by the beam, a good part of the power is dispersed and on the skin of the patient only 14.9 mW are provided.
The duty cycle of the laser is 100%: that means that the laser is continuous and doesn't wait from the end of one sweeping over the bandwidth to the start of the next sweeping process. This is an issue because a brief but not insignificant time is instead needed to pass from one sample point to the next one. There are two solutions: use the end frequency of the bandwidth as the time interval to pass to the next point or skip one sweep of the laser and use that time to pass to the next point. Since we use a short bandwidth, we adopt the second solution: it is slower but no point of the spectrum is wasted.

Looking at the top view of the **reference arm** in Fig. 1.5 we can firstly see the yellow fiber that delivers the light through the system. Once the beam leaves the laser source, it is splitted by the beam splitter (the coupler in the red square) into a beam that goes into the sample arm and another that goes into the reference arm. The ratio 75:25 of the coupler in the Fig. 1.4 shows that 75% of the laser

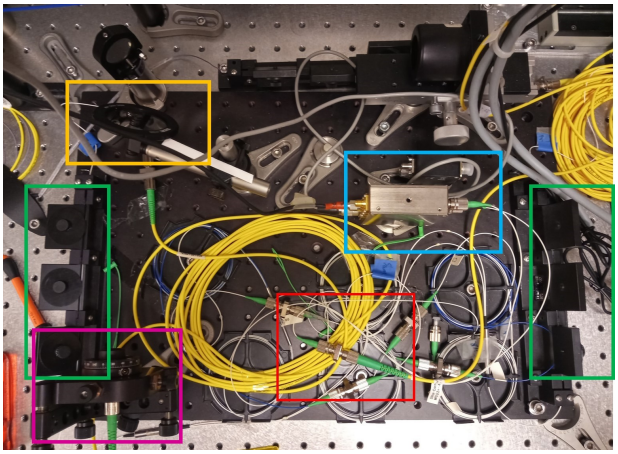

Figure 1.5: Reference arm

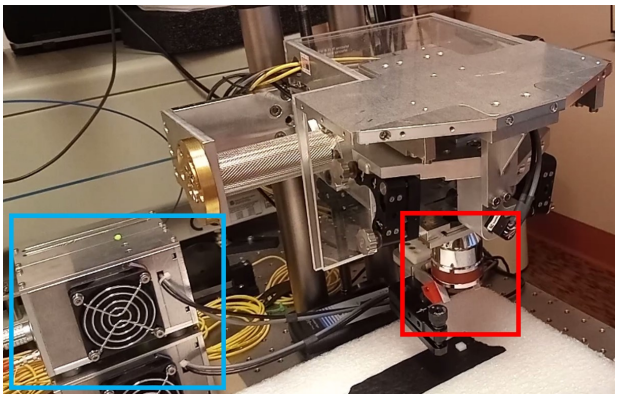

Figure 1.6: Sample arm

power goes into the sample arm and 25% in the reference one.
The reference arm is composed by a collimator (purple square) and 3 pedals (green square on the left) for polarization matching, a wheel (yellow square) for power adjustment and 2 mirrors. Once the beam has reached the end of the reference arm, it comes back through the same path until it meets another coupler where it combines again with the beam coming from the sample arm. After the two beams have recombined, the resultant signal is detected by a dual balanced photodetector (blue square) and sent to the workstation. In particular a dual balanced photodetector is composed of two balanced photodiodes. Matching the two photodiodes results in an excellent performances.

On the other side, Fig. 1.6 shows the components of the **sample arm**: the

galvanometer scanner (green square) and the scan lens (red square) under which the sample is positioned. The galvanometer scanner is a combination of moving mirrors, used to scan the sample automatically in both lateral directions. The 3 pedals for polarization matching in the green square on the right of the Fig. 1.5 also belong to the sample arm. It is possible to change manually the inclination of the beam over the sample.

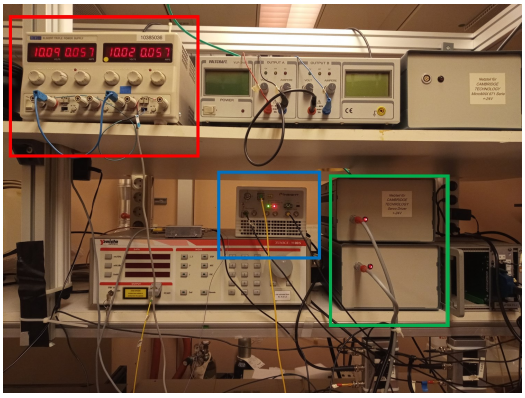

Figure 1.7: Laser source (blue square), power supply to the galvo scanner (green square) and power supply for the detector (red square).

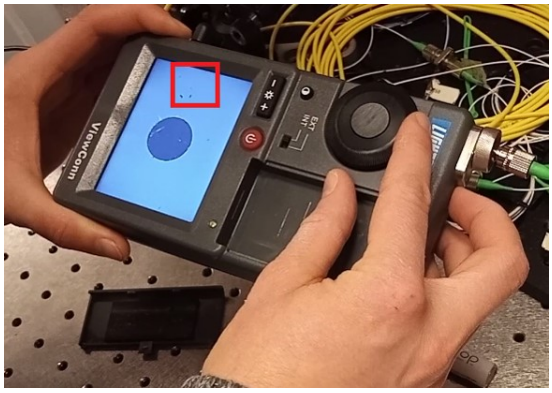

Figure 1.8: Fiber cleaning set up

Lateral and **axial pixelsize** in air were calculated. For the first one, a piece of glass with highly reflective dots on it, called *1mm dot-target*, was used as a sample; since the sample shows a rectangular pattern with 1mm distance between the dots, it was possible to calculate on the resulting image a lateral pixelsize of 19.5 μm. The same process enabled to observe an axial pixelsize of 13.7 μm, but using instead a 1mm thick glass. It is usually good practice to try to have a pixelsize a little smaller than the resolution, which on the other hand depends on the spectrum (axial resolution) and on the optics (lateral resolution).

For the **SNR measurement** I used a simple mirror as a sample and a neutral density filter between the beam and the sample itself. The purpose of the neutral density filter was to reduce the resulting signal of 47 dB, to not damage the system and to not over saturate the signal. Assuming I the detected intensity values and B the background signal:

$$SNR = 10log\left[\left(\frac{max(I)}{std(B)}\right)^2\right] = 105.3dB = (58.3 + 47)dB. \tag{1.13}$$

The background signal is detected by blocking physically the path of the beam in the sample arm.

Two important procedures are useful to maintain the system in its best operating conditions:

- **Fiber cleaning**
  Thanks to the fiber microscope shown in Fig. 1.8 it is possible to identify the dirty parts of the fiber (highlighted by the red box) and then to clean them with a special tissue.
- **Control of the beam alignment**
  It is performed by adjusting the components of the reference arm until the power detected by the powermeter is at its maximum level.

Chapter 2

Optical coherence tomography angiography

OCT provides structural information about the tissue analyzed. An extension of OCT called *optical coherence tomography angiography* (OCTA) gives functional information about the tissue vascular network. It is able to visualize the blood vessels in a completely non-invasive way.

2.1 Data format

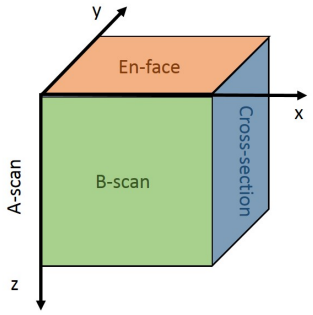

Figure 2.1: Schematic representation of the data format.

Before moving forward it is important to know how the OCT scanning is made. In Fig. 2.1 there is a schematic representation of the scanning directions over the target tomogram obtained after an imaging session.

- An **A-scan** is an unidimensional axial scan in the z direction. One sweep of the swept source laser leads to an A-scan.

- A **B-scan** is a bidimensional scan composed of a series of A-scans collected in the x direction. A B-scan lays on a xz plane. X is called fast scanning direction because the laser scans along that direction firstly whereas it scans over the y direction only after acquiring a complete B-scan. Without surprise y is called slow scanning direction.

- A group of multiple B-scans acquired at adjacent lateral positions (along the y direction) creates the **3D tomogram/C-scan/volume**.

In our acquisitions, each A-scan collects 2048 points even if only around 1500 of them are valid, each B-scan has 512 A-scans and each volume has 512 B-scans.
After collecting all the B-scans it is easy to visualize also the **cross-sections**, bidimensional images on the yz plane. The same procedure can be done to view the tomogram in slices from the top; they are called **en-face** and belong to the xy plane.

Taking 1,43 as the refractive index of the epidermis [5], and considering the axial and lateral pixelsize measured above, the axial and lateral image resolution are $(1.43 \cdot 13{,}7\mu m) = 9{,}6\mu m$ and $19{,}5\mu m$, respectively.

2.2 OCTA techniques

What distinguishes blood from all other tissues? Movement. From the dermatologic point of view, epidermis, dermis and subcutaneous tissues are static, whereas the blood inside the vascular network is the only thing moving.
The basic idea is to acquire **multiple images** of the same tissue location at different timing; the movement of the erythrocytes in vessels and capillaries will be the only thing that make one image differ from the other.

The interferogram provides a spectral profile of the examined tissue area. A fast Fourier transform of it gives information of intensity and phase of the sample. [4]

$$FFT[S(x,k)] = T(x,z)exp[-i\phi(x,z)], \tag{2.1}$$

where S(x,k) is the spectral profile of an A-scan in the k-space and T(x,z) and $\phi(x,z)$ are the magnitude and the phase of its FFT respectively. Motion contrast is obtained by calculating **decorrelation/dissimilarity** between pairs of consequent images. This dissimilarity measure can be made in two main different ways: based on the intensity or on the phase of the Fourier transformed OCT data. In order to increase the SNR of the angiography images an average over the dissimilarity images is made.

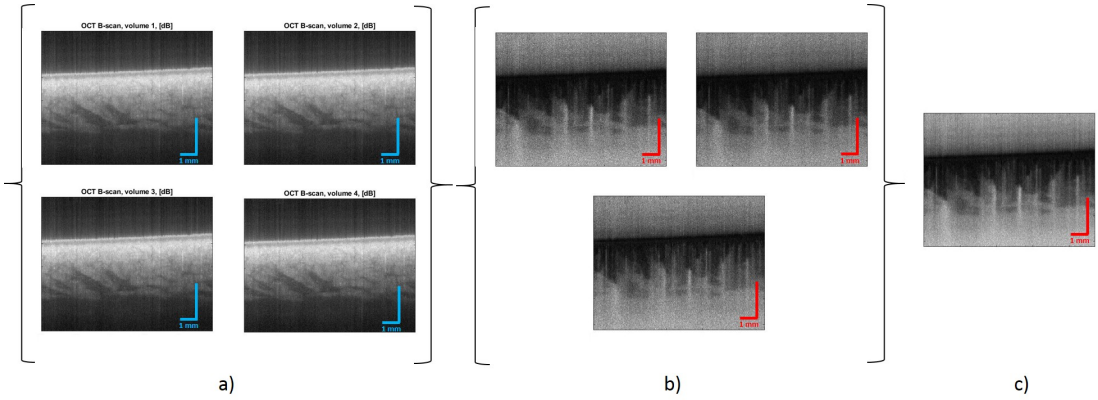

Figure 2.2: Scheme of an OCTA procedure visualized on logarithmic scale B-scans. 4 OCT volumes acquired in different timing (a), pairwise differences between the OCT volumes (b), average between the difference volumes (c).

2.2.1 Intensity based OCTA

This technique takes advantage of the magnitude, T(x,z), of the Fourier transformed data. The motion contrast volume A(x, y, z) is obtained by averaging over pairwise differences of subsequent logarithmically-scaled intensity tomograms log(T(x,z)) from the same set at given position y [4]:

$$A(x,y,z) = \frac{1}{N-1}\sum_{i=0}^{N-1} |log(T(x,z)_{i+1}) - log(T(x,z)_i)|. \tag{2.2}$$

where N is the number of B-scans acquired at the same slow scanning position y at different timing.

It is an easy technique and its main advantage is the low sensitivity to phase noise and trigger jitter. Phase noise and jitter both indicate the stability of the light source, and are interrelated; whenever the signal tends to be instable, the intensity based method is preferred.

2.2.2 Phase based OCTA

In the phase based method the scanning principle is the same but the motion contrast is obtained operating over the phase information, $\phi(x,z)$, given by the Fourier transformed data. The angiogram is obtained by the formula below [4]:

$$A(x,y,z) = \frac{1}{N-1}\sum_{i=0}^{N-1} |\Delta\phi(x,z)_i|, \tag{2.3}$$

where $\Delta\phi(x,z)_i$ is the i-th phase difference between A-scans acquired at the same position y but at different timing [4]:

$$\Delta\phi(x,z)_i = arg\{exp[-i\phi(x,z)_{i+1}]exp[i\phi(x,z)_i]\}. \tag{2.4}$$

Since the phase is sensitive to axial sub-wavelength displacement of the sample, **correction of bulk motion** is required for in-vivo measurements [4]. The correction of the bulk motion takes place by subtracting the circularly averaged phase difference of a single A-scan, $\overline{\Delta\phi}(x)_i$, to the phase difference A-scan itself.

As we have noticed, the phase based OCTA is strongly affected by the bulk motion. Indeed this is the main disadvantage of this technique. Even after the bulk motion correction presented above, motion artifacts are persistant and they show up as white vertical lines in the en-face images. A further weakness is its greater computational complexity. On the other hand, the phase based algorithm is independent of the intensity, so it leads to better contrast results.

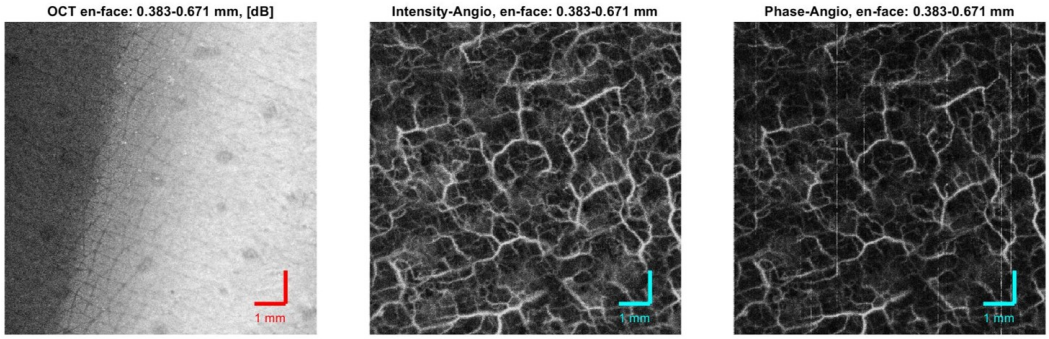

Figure 2.3: Better performances of the phase based OCTA over the intensity based OCTA. Median intensity projection en-face of healthy skin. a) OCT, b) Intensity based OCTA, c) Phase based OCTA.

Not always one method leads to a better image quality in respect to the other. As a proof of that the Fig. 2.3 and 2.4 depicts two different quality performances of the intensity and phase based algorithm.

A further algorithm for the processing of OCTA images is the complex based method. How the name suggests, it takes into account both the magnitude and phase information carried out by the Fourier transformed signal.

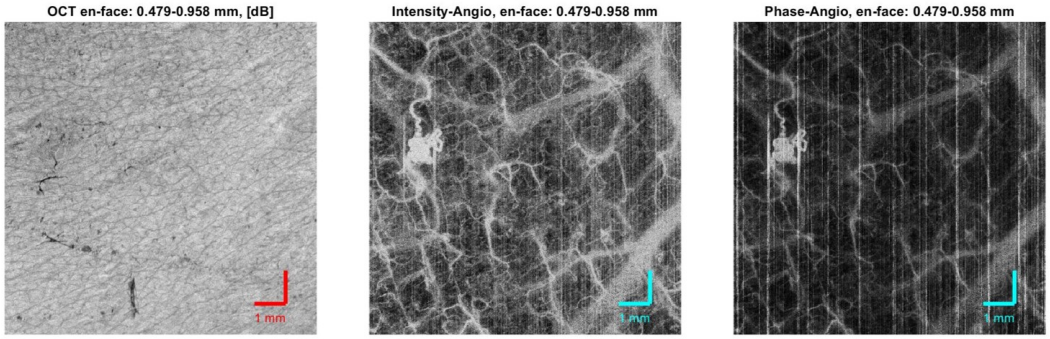

Figure 2.4: Better performances of the intensity based OCTA over the phase based OCTA. Median intensity projection en-face of skin with cherry angioma. a) OCT, b) Intensity based OCTA, c) Phase based OCTA.

2.3 OCTA advantages and limitations

OCTA is not an imaging technique for the quantification of blood flow but it marks the size and geometry of microvasculature. In the following two sections I will present some of the most important aspects that characterize OCTA.

Non-invasiveness

Usually to visualize blood flow, contrast agents are needed. From this point of view, OCTA is revolutionary because it enables the visualization of blood vessels with a good resolution even at the capillary level without any injection of contrast agent in the patient. This avoids all the negative aspects of intravenous injections, such as the long time of the procedure, the invasiveness and any possible side effects of the contrast agent.

In addition the radiations emitted by the laser are non ionizing which means, if properly handled, they are completely safe for the human body.

Interscan time

Since in OCTA N acquisitions have to be performed at the same position, the interscan time between one acquisition and the other is a fundamental parameter to know the sensitivity of the method to the blood flow speed. The interscan time is the time necessary to acquire one B-scan plus the time the scanning needs to return to the starting A-scan position. It is governed by the sweep rate and by the

number of A-scans in each B-scan.

The blood cells moves a distance given by their flow speed times the interscan time [6]. Longer interscan times increase sensitivity to slow flows [6]. In fact, in this case there is enough time to detect in a certain position a blood cell that is moving slowly. On the other hand, long interscan times allow for an increase in motion artifacts. Contrariwise, by shortening the interscan time faster flows can be distinguished and it is more difficult for the signal to saturate, because even faster flows can increase the signal. Slower flows cannot be detected with brief interscan times. A compromise needs to be found.

Considering that the sweep rate is 222.2 kHz and that we acquire 512 A-scans in a B-scan, 512 B-scans in a volume and 4 volumes, the frame rate is $(222.2*10^3)/(512*512*4) = 0.212Hz$. The **acquisition time** of 4 entire consecutive volumes can be easily derived: 4.423 seconds. However the experimental acquisition times are around 20 seconds, due to the long saving times of the dataset itself.

Stability of the ligth source

The more stable the source, the less disturbed is the image. The use of akinetic laser allows a good stability of the light source.

Number of B-scans at the same position

N is an important variable both in intensity and phase based OCTA and it represents the number of B-scans acquired at the same sample location. Increasing it, the resulting image will have an higher contrast, but on the other hand the acquisition session would take longer. Since in my thesis work the target is the human in-vivo skin, high acquisition times lead to a higher probability of motion artifacts. A compromise has been taken into account by choosing N=4.

Wavelength and Bandwidth

In this case, for skin imaging a 1310 nm central wavelength is used because it allows to penetrate deeper in the tissue, until almost 2 mm.

Although a smaller bandwidth (a few dozen of nm) is beneficial for OCTA due to the higher stability with respect to motion artifacts, larger optical bandwidth (one hundred of nm) and thus axial resolution would be desirable for OCT [4]. The system used in this thesis work has a pretty narrow bandwidth (29 nm), in order to prefer robustness over motion artifacts.

Penetration depth

One of the goals of OCTA imaging is the visualization of both the shallower and the deeper vessels of the skin. Unfortunately at larger depth, the image quality degrades dramatically, principally due to scattering artifacts.

This is why new multimodal imaging systems are rapidly expanding in research. An example is the integration of OCTA with photoacustic imaging (PAT). While the first imaging system guarantees a good resolution of superficial microvasculature until about 1 mm, the second has a penetration depth of more than 5 mm despite having resolution limits.

2.4 OCTA Artifacts

Like all imaging techniques, also OCTA imaging is affected by artifacts that degrade image quality, reducing its diagnostic impact. The types of artifacts depend on the application too; in the list below there are the artifacts that may affect an OCTA procedure for in-vivo skin imaging.

Projection artifact

When the light encounter a blood vessel, it may be refracted, reflected or absorbed. The reflected light is detected and is part of the OCTA result, the absorbed one depicts lost information and the refracted one is responsible for the artifact concerned. The transmitted light has time varying fluctuations because it propagates through flowing blood. So the deepest layers are illuminated by this altered light and a false flow is the result.

On cross-sectional angiograms, this artifact appears as the flow tails below in situ blood vessels; on en-face angiograms, the more superficial plexuses are projected on deeper plexuses [7]. In Fig. 2.5 an example of en-face and cross-section affected by projection artifacts is shown. This artifact, also called **decorrelation tail** artifact, makes the visualization of the deeper vessels challenging and gives a false interpretation of the size of the shallower vessels in the depth direction. It is one of the most important artifact in OCTA; I will analyze various methods developed to reduce it.

Galvanometer artifact

The galvanometer artifact is due to the inertia of the galvanometer mirrors. The passage between the galvanometer position at the end of a B-scan to its position at

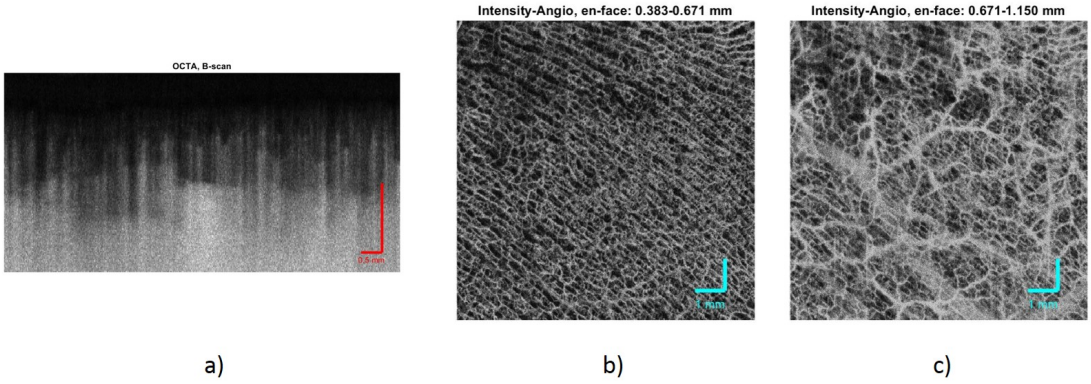

Figure 2.5: Projection artifact on a B-scan view (a)) and on an en-face view (c)). b) is the median intensity projection over a depth interval of 0.383-0.671 mm, while c) is the median intensity projection over a depth interval of 0.671-1.150 mm. In c) we can still see vessels belonging to the b) layer.

the beginning of the following B-scan is not instantaneous; this leads to an artifact at the beginning of each B-scan. An example is shown in Fig. 2.6. The way to eliminate this artifact is to simply delete the cross-sections affected by it.

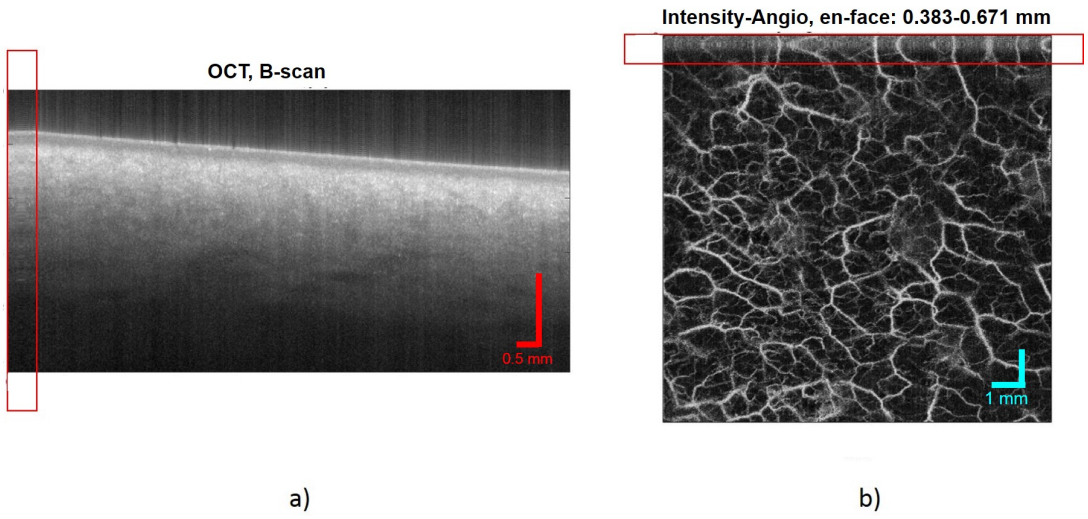

Figure 2.6: Mirror artifact, highlighted by the red rectangle, in a B-scan (a)) and in an en-face (b)) of the same volume sample.

Motion artifact

For in vivo OCTA imaging having motion artifacts is quite common. For skin imaging this type of artifact manifests itself with disconnected splitted vessels or, more frequently, with white vertical lines in the en-face images, as shown in Fig. 2.7. Unfortunately the white line artifact means a loss of information for the entire B-scans affected.

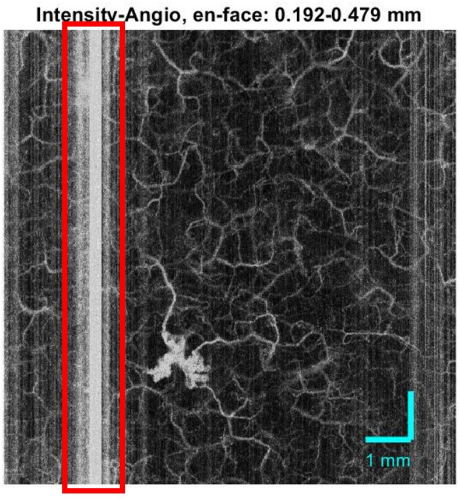

Figure 2.7: White lines artifact (red square) in en-face OCTA images of a cherry angioma and its surroundings.

Attenuation or shadow artifact

Some obstacles can arrest the OCT beam and impede or attenuate the visualization of the underlying tissue or blood flow. A typical example are the hair over the skin (Fig. 2.7). Moreover since a thin layer of water is usually put over the skin sample for refractive index matching, another reason for shadow artifact might be an uneven distribution of the water layer itself. However, care must be taken not to confuse an ill area with actually no blood flow, such as a necrotic tissue, for an actual shadow artifact.

2.5 Reconstruction code

In this section I will present the Matlab code used for OCTA volumes reconstruction. The code developed by me took inspiration from an already existing code [8].

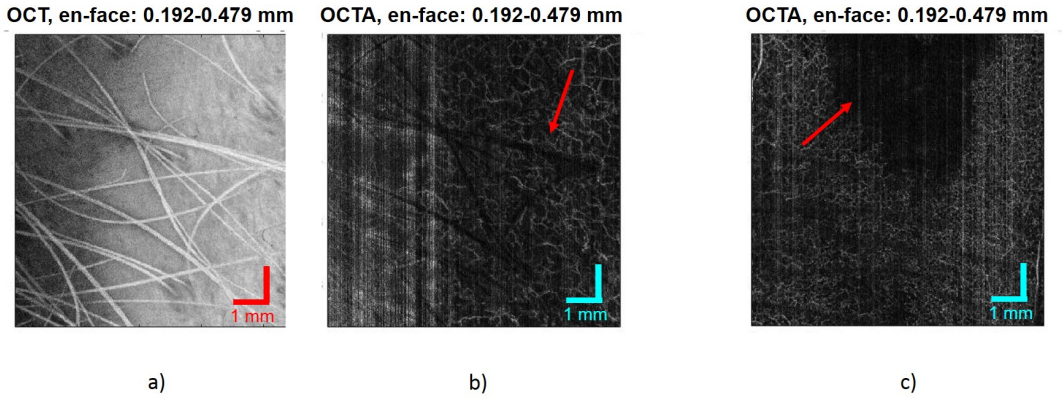

Figure 2.8: The images a) and b) represent an en-face OCT and OCTA image respectively, affected by shadow artifacts due to the presence of hair. Image c) shows an area without blood flow.

The data collected by the OCT system are organized in files, each of them containing the data of 64 B-scans; since the number of B-scans acquired at the same position is 4, each file contains 16 groups of B-scans at different positions. As input the code needs also a *DVV file*; it contains the positions of the valid sweep points of the laser, found through laser calibration. Indeed first of all the **invalid data points** must be deleted from each A-scan.

In order to improve the SNR a **background subtraction** is needed. There are two ways to do that. The first method consists in the subtraction of the mean value of the pixels at the i-th depth level by each pixel at the i-th depth level:

$$A(x, y, z) = A(x, y, z) - \frac{1}{n} \sum_{i=1}^{n} A(x, i, z), \tag{2.5}$$

where n is the number of A-scans in each B-scan.
Another technique for background subtraction is the subtraction from each pixel of the mean of a background dataset. The background dataset is obtained by acquiring a tomogram with the sample arm blocked, so that the camera detects only the background noise and nothing else.

The data are already in the k-space so a re-scaling does not fit in the flowchart. A dispersion compensation is not necessary because the bandwidth of the source is very small. A **zero-padding** is performed to increase the number of data points. Moreover, if the user wants to get rid of some reflection artifacts on the image, he might enable a windowing procedure. Unfortunately this will reduce the images

resolution.

Finally the data is subjected to a **fast Fourier transform** (FFT). Since the FFT creates a symmetric copy of the resulting signal, the removal of half of the output must be done. A further data reduction is performed deleting all the points outside a certain region of interest (ROI) that the user had previously individualized as the prevalent area containing useful information.

At this point a dataset made of complex numbers is obtained. In Fig. 2.11 are presented the flowcharts of the next steps for the OCTA volume reconstruction. First of all the **magnitude** or the **phase** of each complex datapoint of the tomogram is extracted. With a *for-cycle*, N consecutive B-scans are splitted in **N different volumes**; each volume represent an OCT structural tomogram taken at different timing. Due to a saving issue of the system, the last volume needs a shift correction of one B-scan.

In order to remove the noisy pixels in each tomogram, a **mask** can be applied. Pixels that have an intensity greater than a certain threshold or lower than another threshold are removed. The thresholds are choosen based on the histograms of the tomograms. Moreover a selection of the pixels belonging to a restrictive ROI is done to remove the possible presence of the data belonging to the glass.

At this point it is necessary to find the **skin surface points** and transpose them to the zero level of the tomogram. After a median filter applied on each B-scan, the first pixel from the top of each A-scan that overcome a certain threshold is stored in a matrix. The threshold chosen consists of the 85% of the quantile of the A-scan taken into account. The stored points are then fitted to a linear polynomial curve that correspond to the line of the skin surface. By extending the process to all the B-scans, all the skin surface points can be found and translated as they are the first points of each tomogram. In case of acquisitions without glass over the skin surface, the stored points are fitted to a smoother curve line in order to respect the no more flat surface of the skin.

Finally the **Eq. 2.2** for the intensity based OCTA and the **Eq. 2.3** for the phase based OCTA can be converted into the Matlab language and the resulting OCTA dataset can be visualized in various forms: en-face, B-scan or cross-section.

It is also worth reporting the method used for **bulk motion correction** in the phase based algorithm. Since we are dealing with phase angles, the mean of each A-scan is a circular mean. It is implemented in Matlab thanks to the function *circ_mean*. The mean phase angle is then corrected thanks to the function

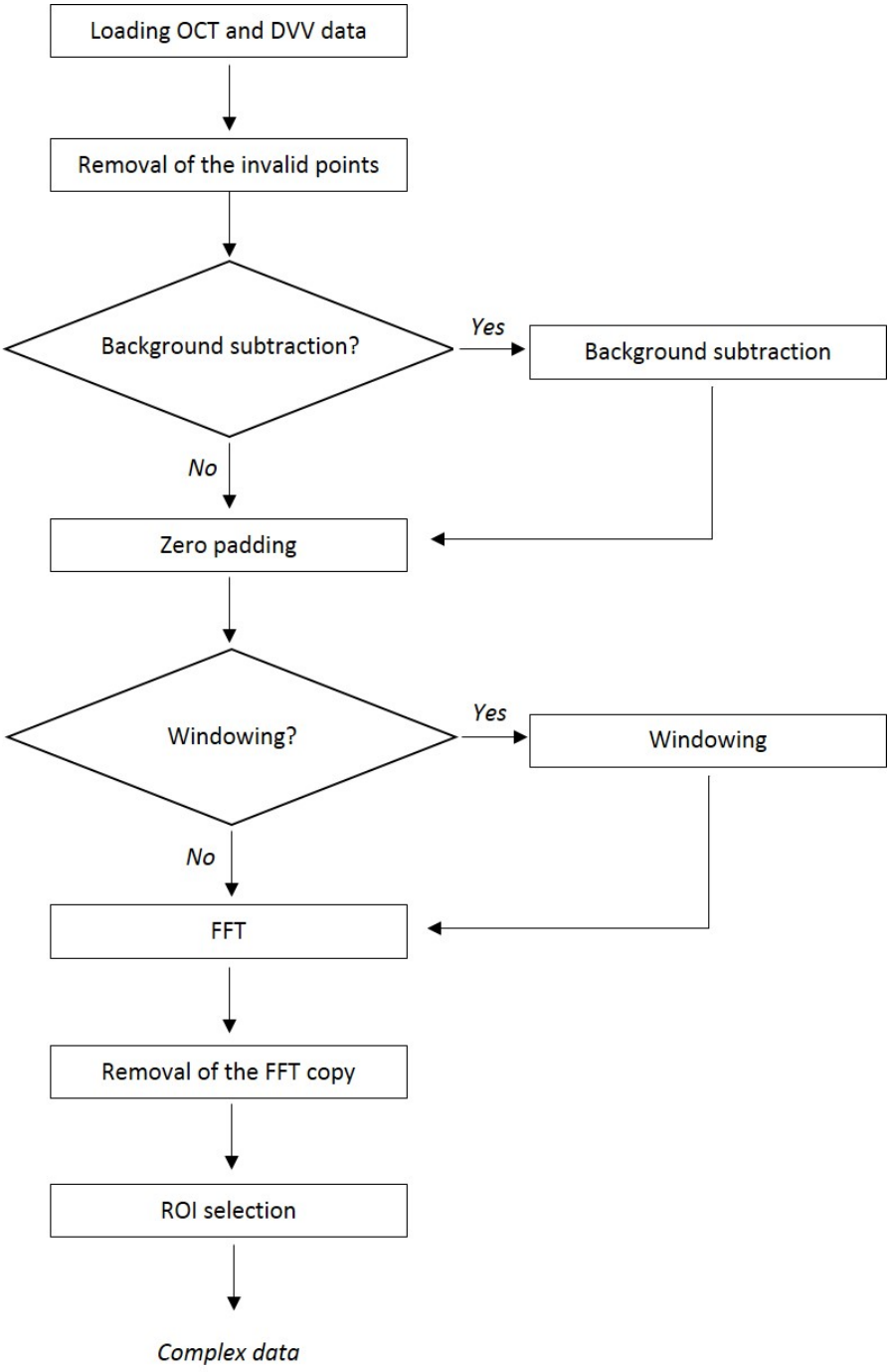

Figure 2.9: Flowchart of the OCT reconstruction code.

unwrap. Whenever the jump between consecutive angles is greater than or equal to

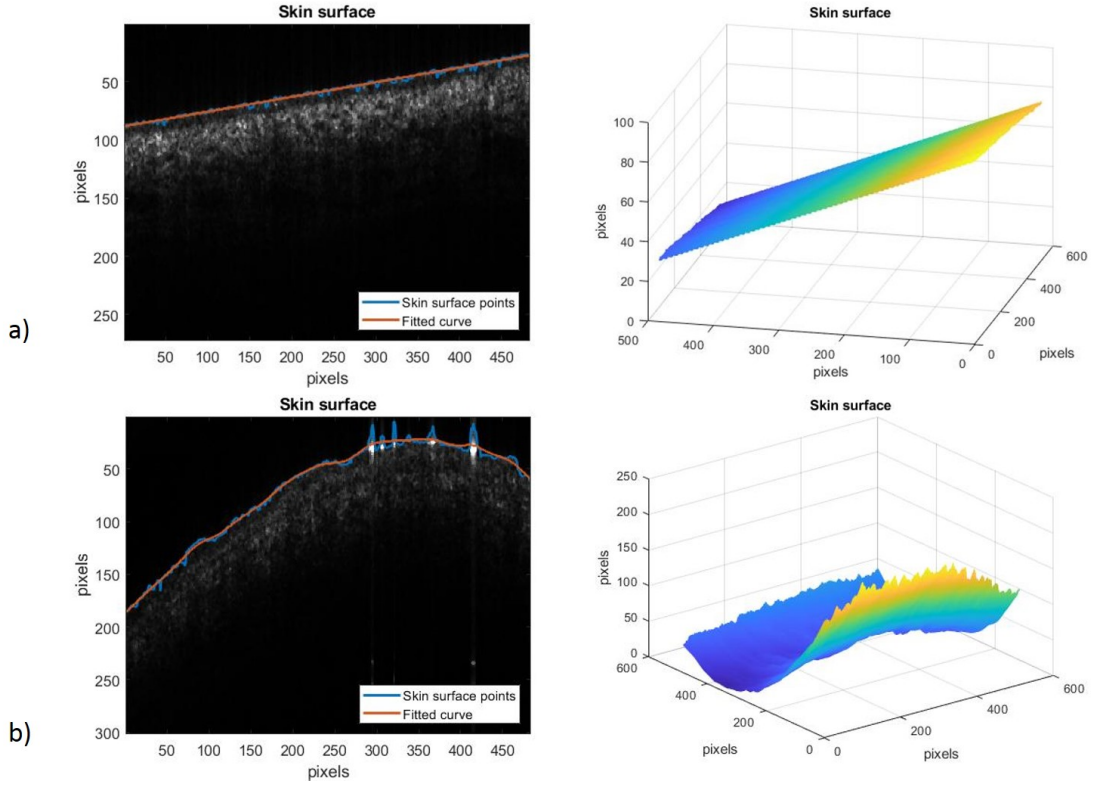

Figure 2.10: Skin surface flattened by a glass over it (case a)), natural curvature of the skin without any glass on it (case b)). On the left side a B-scan and the fitted line of the skin surface points. On the right side a 3D visualization of the points locations of the skin surface over the entire tomogram.

π, *unwrap* shifts the angles by adding multiples of 2π until the jump is less than π.

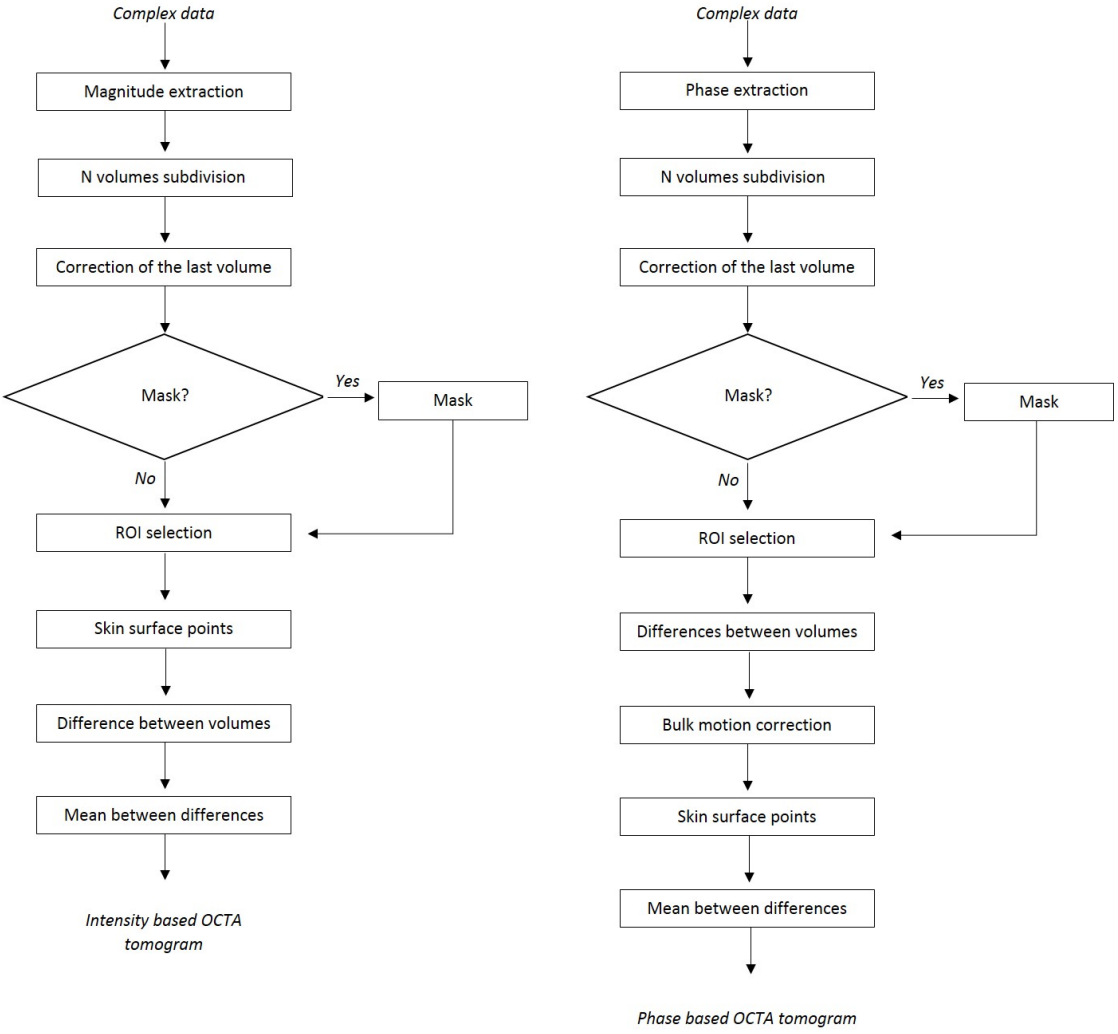

Figure 2.11: Flowchart of the OCTA reconstruction code: on the left side the intensity based algorithm one and on the right side the phase based algorithm one.

Chapter 3

Clinical application

3.1 Clinical target: the skin

The skin is the largest organ of the body, it belongs to the integumentary apparatus and it mainly acts as a protective barrier. It also has an important role in temperature regulation, sensation, balance of fluids and synthesis of vitamin D. It is composed of three layers, listed here from the shallowest to the deepest:

- **Epidermis**
  It can be further divided into sublayers, each of which contains mostly a certain type of cell that fulfils a certain type of function. For example the keratinocytes synthesize keratin, a very stable and resistant protein which main function is protective, the dendritic cells that exert immune-surveillance against external or internal antigens or the melanocytes that gives the skin its color.
  This stratum is very dynamic: cells are constantly dying and being replaced. The deeper you go throught the layers of the epidermis, the younger the cells get. Regeneration happens in the lower layers and new cells move up towards the surface maturing along the way, where they eventually die and slip off the surface of the skin. This happens because the epidermis is epithelial, so it is avascular.

- **Dermis**
  The dermis is where most of the work that skin does gets done, like sweating, circulating blood, sensory feeling. It contains mostly collagen, a structural protein, but also hair follicles and sweat glands. The sensory nerves fibers come up and go all the way up to the base of the epidermis.

- **Subcutaneous tissue or hypodermis**
  It is composed mostly of adipose or fat tissue. Below it a layer of connective

tissue is found. Artery and veins of the skin originate in the subcutaneous tissue area and their projected capillaries go all the way up to the base of the epidermis.

The thickness of each layer depends on several factors but principally on the location of the area investigated. For example the epidermis layer in the palm and in the foot sole is thicker than in other body regions.

The interaction between the skin and the investigating light beam of the OCT system leads to a certain signal that depends on the composition of the skin itself. The outcome on the image can be:

- dark or darker relative to other regions if the scattering area is **hypo-reflective**. This happens when the beam hits basal cells, blood, layered keratin and keratinised cells.

- bright or brighter relative to other regions if the scattering area is **hyper-reflective**. Epidermal keratinocytes, collagen, keratin deposits, dense keratin are structures that give an hyper-reflection.

Also the color of the analyzed skin is a factor that can influence the OCTA signal: darker skin absorbs more light. This results in a less scattering and low outcome signal.

After this **considerations**, we can explain why on the OCT volumes the vessels appear darker than the other structures and why the OCTA volumes don't contain vessels information until about $200\mu m$ under the surface of the skin. Usually between $200\mu m$ and $600\mu m$ a layer of microvasculature of tens of μm of diameter can be seen whereas underneath bigger vessels of about hundreds of μm are detected. Of course the thickness and the composition of the skin layers varies, so that different kind of vascular networks might be observed in different patients and different locations.

3.1.1 Skin lesions

Due to the Covid restrictions the avaiability of patients that could have undergone the OCTA imaging was compromised. In this thesis all the data belongs to healthy skin tissues or to the following types of lesions belonging to volunteers: wounds, seborrheic keratosis and cherry angiomas.

Wound healing

The wound-healing process consists of four highly integrated and overlapping phases: hemostasis, inflammation, proliferation, and tissue remodeling or resolution [9]. The hemostasis phase is characterized by vascular constriction and coagulation. Afterwards the wound area is cleansed of dead cells and external microbes by lymphocytes, neutrophils and macrophages which play a key role in the inflammation phase. The proliferative phase is distinguished by a re-epithelialization of the wound, associated with the promotion of angiogenesis. The main events of this phase are the production of extracellular matrix, vascular growth and expansion of granulation tissue. Finally, the last phase consists in the resizing of the vascular density in the area of the lesion. The remodeling phase could last also for years.

There are many factors that might influence the wound healing process. Some of those are systemic, such as age, sex hormones, obesity, stress, smoking and alcohol consumption and in general poor tissue oxigenation. Other causes of impaired wound healing are related to diseases, like diabetes or venous stasis disease, and could lead to chronic wounds also called ulcers.

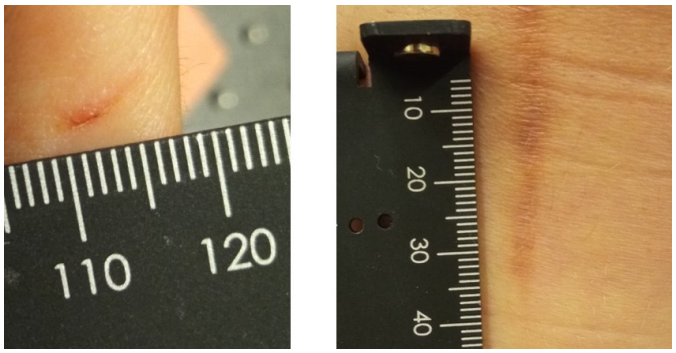

Figure 3.1: On the left a wound at the early wound healing stages, on the right an already healed wound.

Seborrheic keratosis

One of the commonest benign epidermal skin tumor is the seborrheic keratosis. It is caused by the benign proliferation of immature keratinocytes, resulting in well-demarcated, round or oval, flat-shaped macules [10].

The diagnosis takes place thanks to an overall dermatological examination of the interested area. The lesion presents an opaque and verrucous surface and it can occurs in different colors, shapes and sizes.

They usually does not require any treatment considering they are benign lesions. However, especially if they are in uncomfortable areas, they can become inflamed and lead to erythema, pain and bleeding. In this case the removal of the skin lesion is recommended. Moreover a removal procedure is taken into account if the seborrheic keratosis rapidly changes its sizes and aspects and suspiciously bleeds, because it could reveal a suspected malignancy. Cryotherapy, shave excisions and electrodesiccation are the mostly used treatment techniques for seborrheic keratosis.

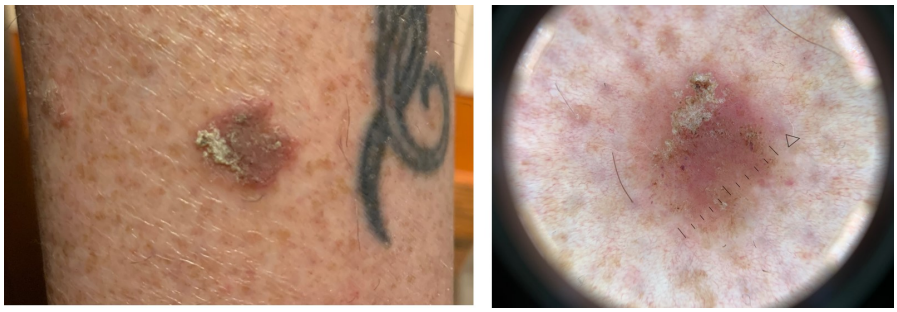

Figure 3.2: Seborrheic keratosis.

Cherry angioma

Another very common type of benignant skin lesion is the cherry angioma, also named *Campbell de Morgan spots*. They are dome-shaped, small (0.1 to 0.5 cm in diameter), bright red to violaceous, soft, compressible papules with smooth surfaces that blanch with pressure and bleed profusely with traumatic rupture [11].

They occurs more with advancing age, by genetic reasons or due to the exposure in the long term to certain drugs and chemicals. No treatment is taken into consideration because cherry angiomas are benignant and asymptomatic skin lesions. The removal of the lesion can be performed through electrodesiccation or laser ablation for aesthetic reasons.

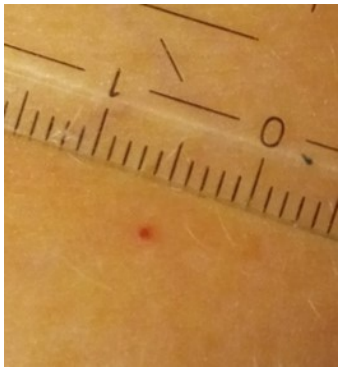

Figure 3.3: Cherry angioma.

3.2 Vascular patterns

Nowadays usually the diagnosis of the skin lesions are done with dermoscopic imaging techniques. They allows to analyze the **morphological structure** of the lesion and evaluate the specific internal structures that constitute it.

Often, however, morphological analysis of the lesion does not allow for an analysis of the vascular network within and around it. The **vascular analysis** can be very useful in the distinction between healthy and diseased skin and in the classification of the type of the lesion itself. For example, with only morphological analysis of malignant lesions, the borders of the lesion outlined for its removal are not accurate and the patient must eventually undergo a second surgery for a better resection.

What are the information that we can extract from a vascular analysis? It is known that in general a **malignant lesion** differs from a benignant one because it has:

- a more dense and chaotic vascular network,
- more vessels with more messy branches,
- a wider range of vessels diameter and
- a higher vasculature tortuosity.

In fact, since the tumors promote the angiogenesis in order to grow faster, most of the tratment anti-tumor are also anti-angiogenic.

Also the morphology of the vascular structures and the structural arrangement of the vessels may depend on the type of lesion. Some dermatologic studies have identified the following **vessels morphology type** classification:

- arborizing vessels,
- pinpoint or dotted vessels,
- hairpin-like or linear looped vessles,
- comma-like or linear curved vessels,
- linear vessels,
- glomerular vessels,
- crown vessels,
- polymorphic vessels,
- strawberry pattern,
- milky red globules or clods,
- red globules,
- twisted red loops
- spermatozoa-like vessels

and the following **structural patterns of vessels**:

- regular,
- string-like,
- clustered,
- radial,
- irregular arborizing,
- reticular,
- irregular or non-homogeneous [12].

Let's focus briefly on the vascular characteristics that affect the lesions analyzed in this thesis.

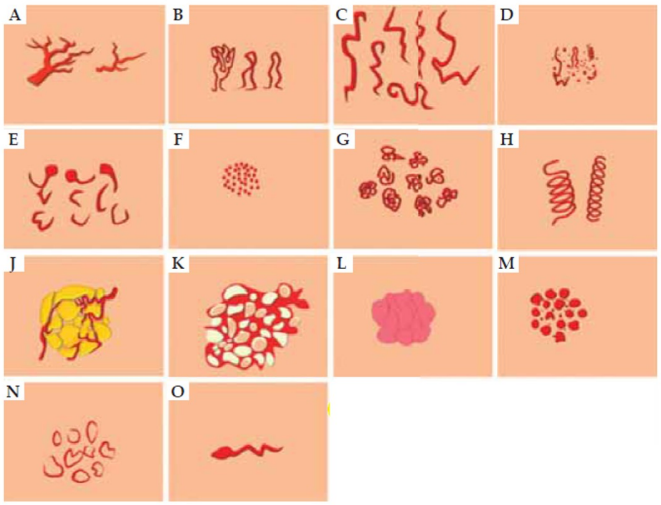

Figure 3.4: Morphological vessel types. Arborizing (A), hairpin-like (B), linear (C), polymorphic (D), comma-like (E), dotted (F), glomerular (G), corkscrew-like (H), crown-like (J), strawberry pattern (K), milky red globules (L), red globules (M), twisted red loops (N), spermatozoa-like vessels (O). [12]

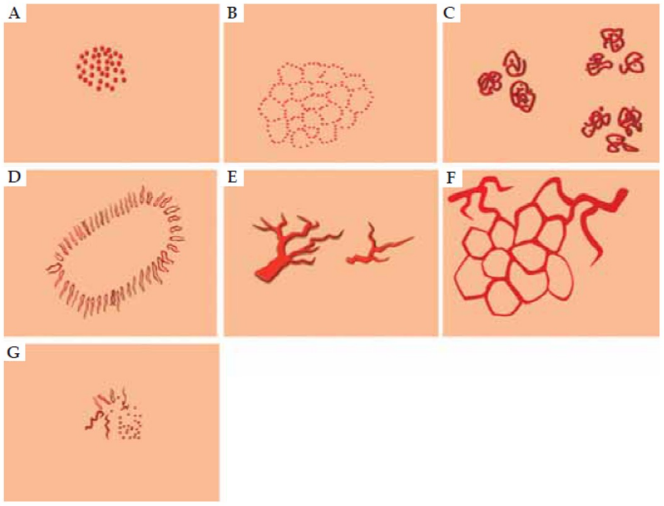

Figure 3.5: Structural arrangements of vessels. Regular (A), string-like (B), clustered (C), radial (D), irregular arborizing (E), reticular (F), irregular (G). [12]

Wound healing

It has already been mentioned that in the early stages of the wound healing process a new capillary network takes place within the lesion. Angiogenesis factors such as FGF and VEGF are produced to a greater extent, so that new capillaries form

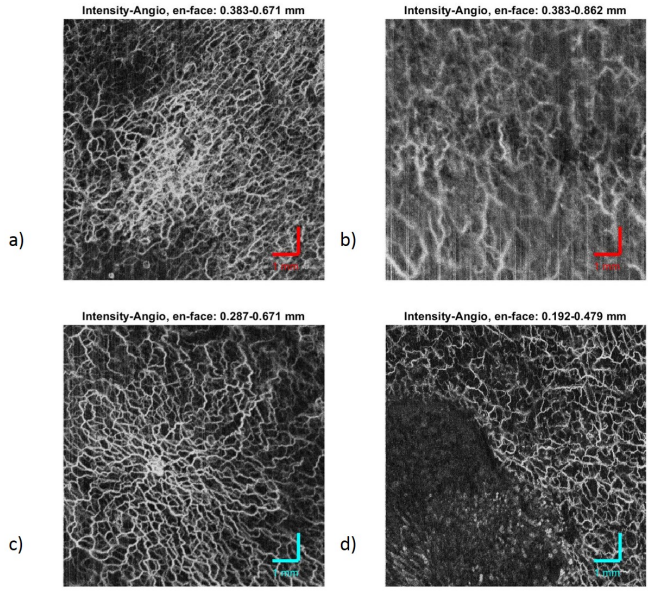

Figure 3.6: Median intensity projection OCTA en-face of: not healed wound (a)), healed wound (b)), seborrheic keratosis (c)), cherry angioma (d)).

and migrate into the concerned site. Capillary sprouts eventually branch and join to form capillary arcades through which blood flow begins [13]. Whereas in the last phase of the healing, the new vascular network previously created decays into apoptosis and the skin area is replaced by scar tissue.

The wound investigated with the OCT system in this thesis was a little cut 2 days old on the finger of the patient (Fig. 3.1 on the left). This means that we still expect to see an increase of the vascular density within the skin area affected (Fig. 3.6 a)). The other wound analyzed was, instead, already healed and the vascular network seems to be more regular (Fig. 3.1 on the right and Fig. 3.6 b)).

Seborrheic keratosis

Looped/hairpin vessels are often associated with seborrheic keratosis and may be of additional diagnostic value. Hairpin vessels can occasionally be observed in other skin tumors such as keratoacanthomas, basal cell carcinomas, and melanomas.[14]

Seborrheic keratosis are usually characterized by regular hairpin-like vessels and/or *dotted* vessels. Those are vertically arranged capillaries homogeneously distributed; they are *U-shaped* and they have approximately the same diameter of about 0.01-0.03 mm. Fig. 3.2 and 3.6 c) shows pictures and OCTA representation

of the seborrheic keratosis analyzed in the laboratory.

Cherry angioma

In cherry angiomas is evident a *clustered red globular* configuration of the vasculature. In fact, from the vascular point of view they appears as clusters of capillaries just below skin surface. Fig. 3.3 and 3.6 d) shows s picture and an OCTA representation of one of the cherry angiomas analyzed in the laboratory.

3.3 Patient imaging

3.3.1 Imaging protocol

In this section I'll expose the protocol that I applied for the patient imaging sessions. The imaging protocol is is a set of rules and procedures that must be followed in order to obtain the best performance of the entire process. After various tests and experimental trials it has been noticed that the best way to approach an imaging session is by following the steps below.

1. **System calibration**
   First of all a calibration of the laser must be done. The light source is regulated in order to improve its accuracy. The procedure is attuated by an apposite software created by the producer (*Insight*). As a result, position of the valid sweep points of the laser are found and stored in the already discussed *DVV file*. This step must be done each time the laser is turned on.

2. **Safety measures**
   Two types of safety measures are taken into account:

   - Since the acquisitions were made during the Covid-19 pandemic, the sessions must be made in accordance to the safety measures adopted by the Medical University of Vienna against the virus.
     A disinfection of all the instrumentation must be done and both the operator and the patient must wear an FFP2 mask.
   - The laser used is a class 3B light source. This means that some precautions must be taken. In particular the subject must be provided with protective glasses against the laser beam that in our case utilizes a central wavelength of 1310 nm.

I would like to mention that as stated in the *International standard - safety of laser products - IEC 60825-1*, the maximum permissible exposure (MPE) of the skin to laser radiation in the range of wavelegnth 700-1400 nm for an exposure time of $10 - 10^3$ s is:

$$MPE = 2000 \cdot C_4 \, Wm^{-2},$$

where C_4 is a correction factor equals to 5 for our wavelength range. Moreover since the size of the skin area investigated is about $1cm^2$, the MPE become:

$$MPE = 1 \, Wcm^{-2}.$$

The power provided to the patient in our applications stays widely under this value.

3. **Patient setting up**
   The patient is positioned on a comfortable chair or bed and the interested area is located facing the probe. A vacuum cushion can be also adopted for the purpose: when it is in the normal state it adheres to the patient leg or arm and after the removal of the air it turns into a rigid shape that prevents the patient movement.

   A 1 mm thick glass is placed between the skin area and the probe in order to avoid the hyper-reflection of the surface of the skin. It is important to tell that the entire skin surface has to be in contact with the glass. Moreover some distilled water is distributed between the glass and the skin to allow a better refractive index matching between those two. The more uniformly the water is distributed, the better.

   One last check is done with an *infrared viewing card*. This is helpful to control that the laser beam will investigate the correct skin area.

4. **Data quality improvement**
   Once the sample is exposed to the laser beam a preview of a B-scan of the volume is displayed on the workstation. Some adjustments can be performed by the operator on the system in order to enhance the quality of the image shown and as a consequence of the acquired data:

   - **Change of the beam tilt**
     Since the hyper reflections emanating from the skin surface are maximum when the beam is perfectly perpendicular to the skin surface, a slight tilt of the investigating system from the vertical axis allows to reduce their intensity.

- **Focus positioning**
  With the help of two gears the depth of the focus in the sample and the distance between the sample positioning area and the sample can be adjusted as desired.
  Usually the focus is set slightly below the skin surface, where the majority of the vessels that can be detected by the system are. Moreover is a good practice not to apply too much pressure on the patient's skin with the slide while maintaining constant contact between slide and skin over the entire area to be investigated.
- **Contrast enhancement**
  By rotating the wheel for power adjustment some changes in the contrast of the previewed image can be seen. Higher contrast is usually preferred even if it is crucial not to saturate the signal.
- **Artifacts attenuation**
  The only type of artifact that the preview image shows is the high reflections that the skin surface projects back to the detector. The glass positioned on the skin and the tilt of the beam are already helpful to reduce them, but for a more accurate image acquisition the pedals for polarization matching should be adjusted. Particular attention must be paid as the beam may misalign during this process and therefore give poor quality results. If this happens also the collimator needs to be aligned for the maximal power.

Unfortunately we are not able to quantitatively know when the combination of these measures gives the best results, but we can only get an estimate of the quality of the data by looking at the preview image after each adjustment step.

5. **Acquisitions**
   At this point the acquisition can start. Each acquisition takes about 20 seconds. Considering that we don't know in advance the quality and the artifacts that affect the data we are acquiring, it could be a good practice to acquire multiple times the same OCTA volume in different conditions. The procedure attends the following steps:

   - **Galvanometer exchange**
     Two acquisitions are made after exchanging the fast and slow scanning direction. We will see in the next chapter that those two acquisitions will help attenuate the eventual motion artifacts.
   - **Depth of focus**
     Several acquisitions are made after changing the depth of focus.

- **Acquisition without the glass**
  If the shape of the investigated area doesn't allow a good attachment between the skin and the glass, an acquisition of the skin without any glass is made.

6. **Picture of the lesion**
   It is useful to keep a record of the lesion scanned with a picture of it juxtaposed by a ruler. This will help to remember the location and the dimension of the lesion.

7. **Background acquisition**
   The background noise is then acquired by blocking the beam of the sample arm with a simple cardboard.

3.3.2 Experimental tests

Several experiments were carried out in order to find the set up that permits the best imaging performance.

Lesion location

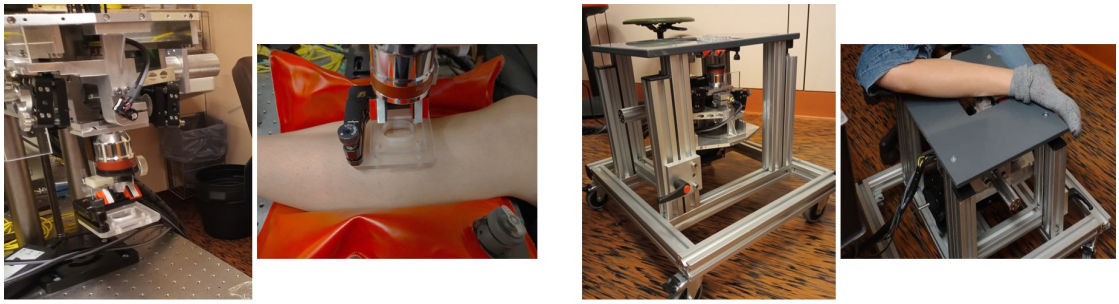

Figure 3.7: a) System and patient positioning for lesions on the anterior leg and arm. b) System and patient positioning for lesions on the posterior leg and arm.

The system was originally positioned as in Fig. 3.1 a), but that is difficult for imaging lesions that appears on the posterior part of the patient body. For this purpose a different arrangement of the system was designed. As show in the Fig. 3.1 b) the system is rotated upside down, positioned on a cart and the sample is placed over it.

Type of glass

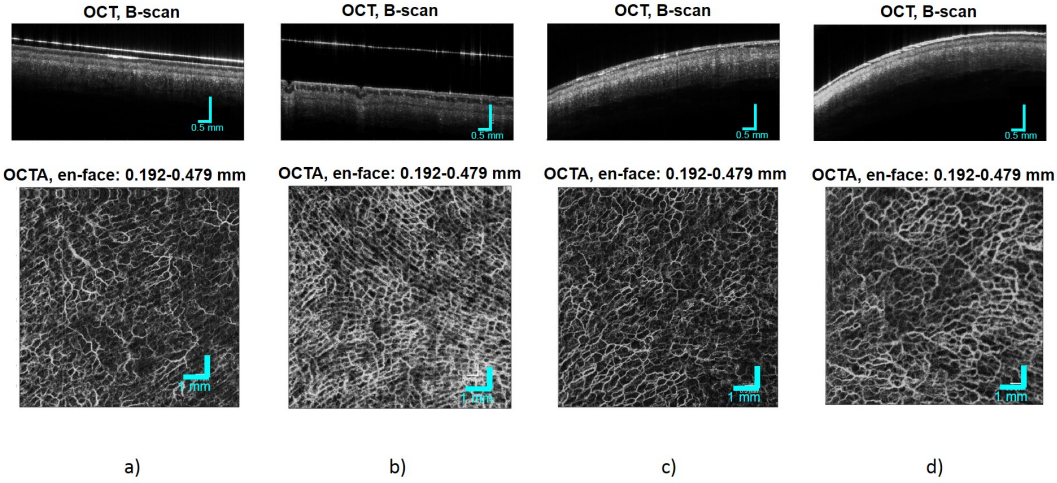

Figure 3.8: B-scan and en-face intensity based OCTA images from a palm healthy skin sample using a 0.1 mm thick glass (a)), a 1 mm thick glass (b)), a plastic foil (c)) and leaving the surface of the skin free (d)). The skin area analyzed slightly changes position between the acquisitions trials.

One of the drawbacks that is easy to run into during the acquisition is the interaction between the glass and the target skin, especially if the lesion is placed in a non easily reachable or in a bony part of the body. For this reason those type of tests were performed:

- Contact of the skin with a **1 mm thick glass**
- Contact of the skin with a **0.1 mm thick glass**
  The thickness of the glass does not influence significantly the performance of the image acquisition session. On the other hand the acquisition with the thin glass was even more uncomfortable so the technique was abandoned.
- Contact of the skin with a **plastic foil**
  A plastic foil seemed to be the appropriate solution to mitigate skin surface artifacts and to be comfortable for the patient.
- **Direct contact** of the skin with the investigating beam
  Another test was done without any medium in the beam path before impacting on the skin. In this case the back reflections of the skin are relevant and disturbing for the images.

The last two acquisition modalities were discarded because they did not allow to have a flat surface of the target skin area. Since the focus is placed at a defined depth level, it was difficult to keep an entire skin layer in focus. As a consequence, often parts of the en-face images results with less vessels or with a lower resolution in respect to the rest.

After several acquisitions tests we choose to continue the clinical ones with the 1 mm thick glass.

Pressure applied

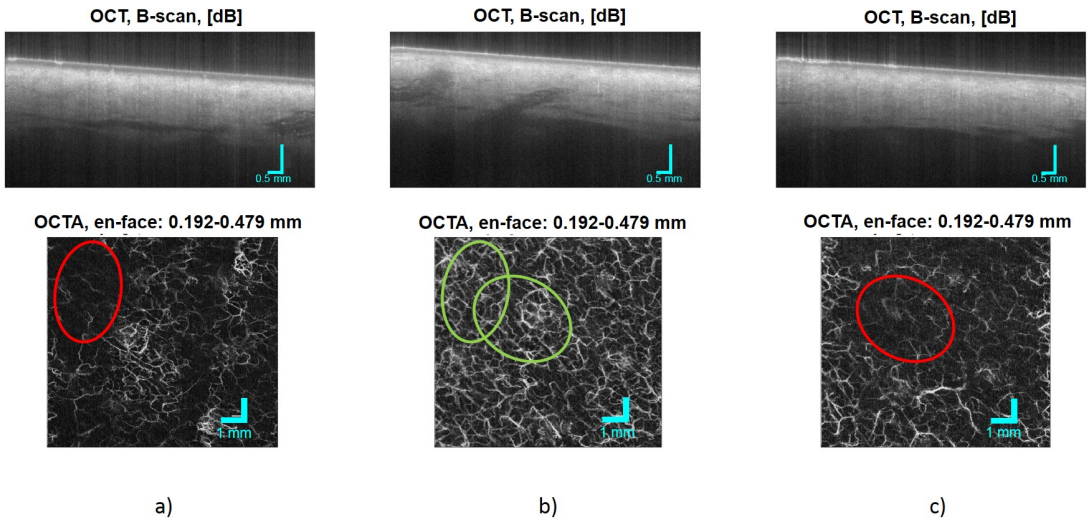

Figure 3.9: Influence of the pressure applied on the sample on the OCTA image quality. From the left to the right more pressure was applied. On the top the MIP of the B-scans in the logarithmic scale; on the bottom the MIP of the en-face in the depth interval between 192 and 470 μm.

It was noticed that in a lot of acquisitions made on healthy skin, some areas showed a very low vessel density. This was not clinically explainable. In Fig. 3.9 are displayed the cases of the same healthy skin volume under three different pressure conditions:

- In the **case a)** a low pressure is enforced against the glass and various areas on the en-face image do not show vascular patterns. This is due to a non perfect contact between the skin and the glass.

- The **case c)** presents the same issue this time due to an higher pressure between the sample and the glass that obstacle the blood flow in the capillaries.

- The performance increase significantly when the sample laid over the entire glass without extra pressure on it. In **case b)** the green circles highlight the presence of vessels that in the cases a) and c) were not detected (red circles).

Depth of focus

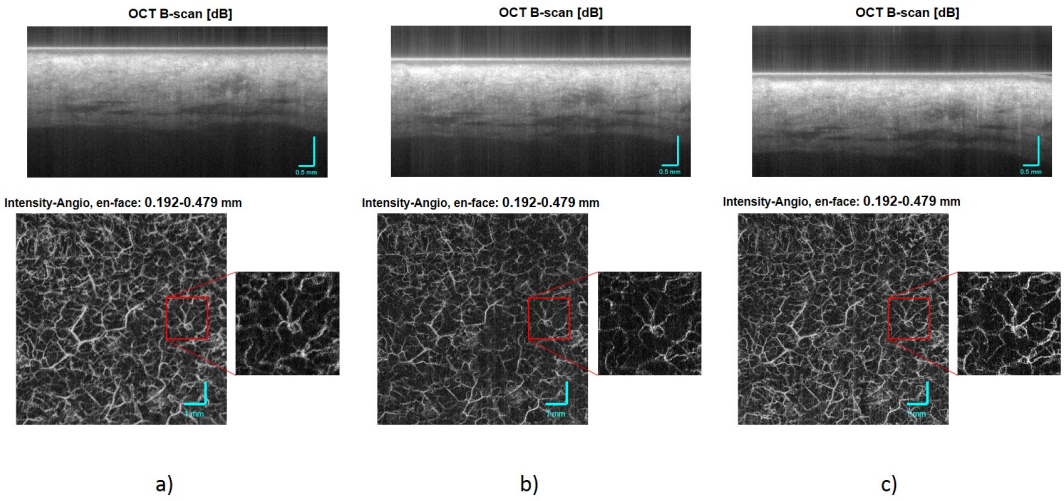

Figure 3.10: Influence of the depth of focus. From the left to the right the focus is positioned increasingly shallow.

As we already mentioned, the thickness of the skin layers varies meaningfully according to the location of the lesion and to the subject itself. For this reason there isn't a common rule that allows to identify a depth level at which the majority of vessels are and as a consequence at which the beam should be focused.

This is why the imaging protocol presented in this thesis includes various acquisitions where the beam is focused at various depth. In the Fig. 3.10 we can notice for example an increase of the vessel resolution with a shallower depth of focus (case c)).

Chapter 4

Image processing

Once obtained the angiography tomogram, it is important to perform on it some operations in order to have a better quality of the images and afterwards to extract some useful information from them. In the flowchart in Fig. 4.1 are shown the steps implemented for the image processing of the OCTA tomograms.

4.1 Artifacts removal

As already mentioned, the intelligibility of OCTA images is severely compromised by artifacts, especially by projection artifact and by motion artifact. If no corrections were made to reduce those artifacts, the information subsequently obtained from the segmentation of the lesions would be falsified.

4.1.1 Projection artifact removal

In literature there are already some methods to attenuate the projection artifacts but the applicability of a certain method depends also on the type of dataset we are dealing with.

Firstly a simple **slab-subtraction-based algorithm** [7] was proposed: the en-face layer affected by the artifact is subtracted from the en-face layer above. This works pretty good when the sample has clearly defined layers of vascular network, such as the vascular pattern of the eye. Unfortunately the skin doesn't have a precise subdivision in layers of its vascular network. Consequently the method doesn't fit.

Mean subtraction method is also used to remove the tail artifacts, following

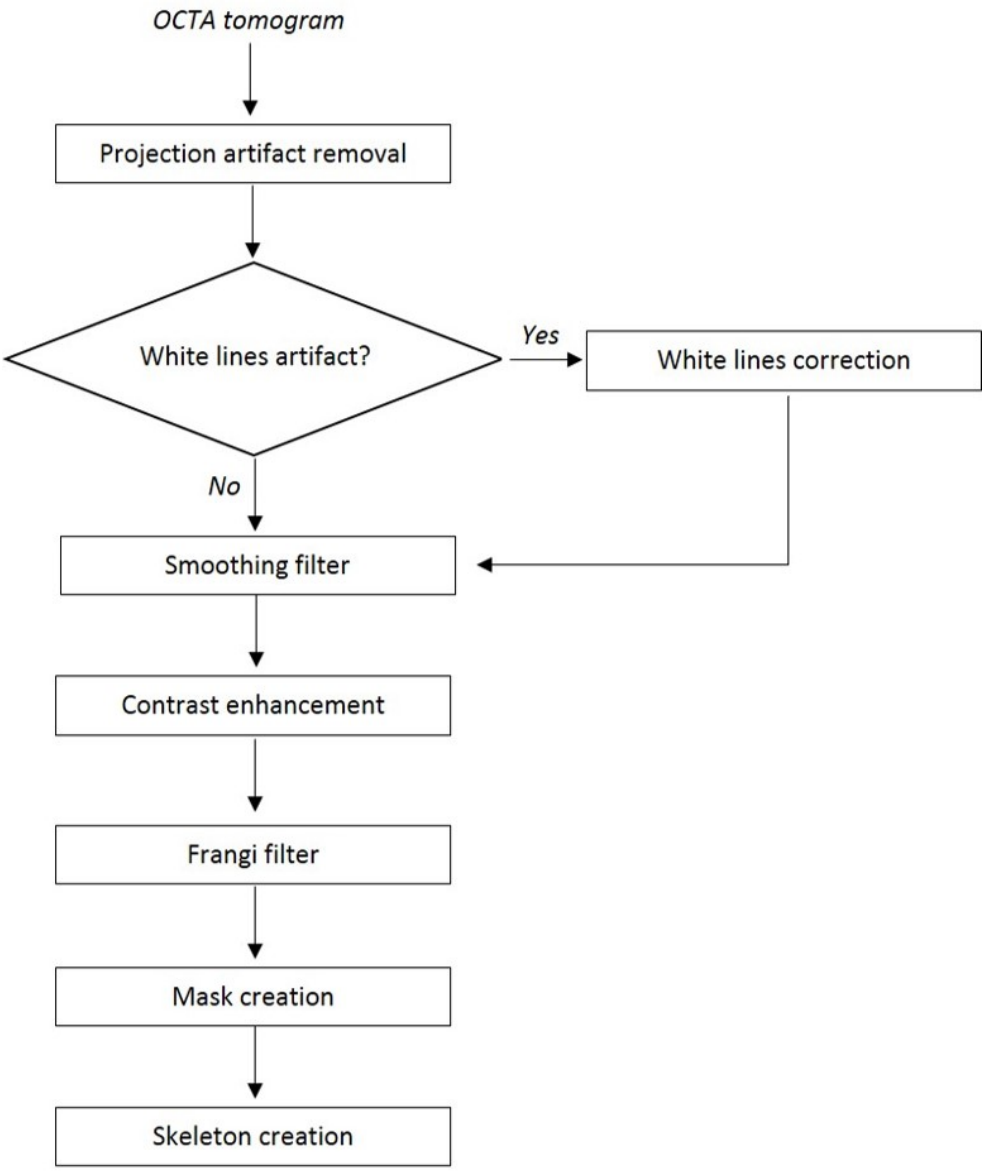

Figure 4.1: Flowchart for OCTA image processing.

the equation:

$$A_{corr}(x,y) = A(x,y) - \omega \times \frac{1}{N}\sum_{k=1}^{N} A(x,y,k), \tag{4.1}$$

where $A_{corr}(y,z)$ and $A(y,z)$ are an A-scan of the projection resolved OCTA tomogram and the original OCTA tomogram respectively and N is the total number of pixels in an A-scan. k denotes the k-th depth position in an A-scan and ω is a weight applied to the mean term, previously chosen by the user; high ω values correspond to a higher attenuation. This algorithm depends on the total intensity in each A-line, and would thus be increasingly aggressive for A-lines with longer tails [15]. From the Fig. 4.2 we can notice that the decorrelation tails are quite long in skin imaging. Hence, using a subtraction method based on the mean will retain the signal strength for deeper vessels [15]. In fact, the information of the shallower vessels are lost with this technique.

The method that seems to be the most adequate, in our case is the **step-down exponential filtering** [15]. The technique follows the rule:

$$A_{corr}(x,y,z) = A(x,y,z) \times e^{-\frac{1}{\gamma}\sum_{k=1}^{z-1} A_{corr}(x,y,k)}, \tag{4.2}$$

γ is, likely ω for the previous method, a constant attenuation parameter. As the Fig. 4.3 shows, with $\gamma = 0$ no change is produces in the B-scan, whereas increasing the value of the constant, a higher attenuation of the tails is performed. Keep in mind that too high values of γ lead to attenuation also of the useful blood flow information.

In the Fig. 4.2 the results of the three methods applied on the OCTA dataset of an healthy skin sample are shown. The best performance and the higher information retention are depicted by the step down exponential method.

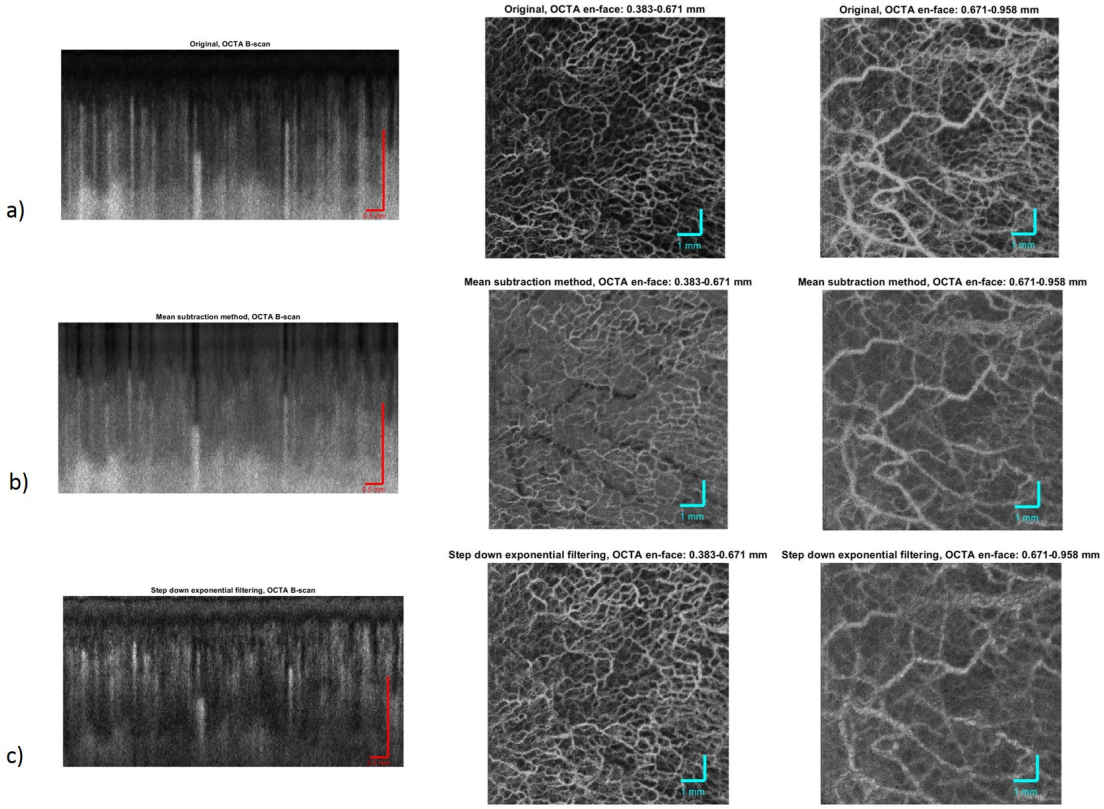

Figure 4.2: Projection artifact removal: a) Original B-scan and en-face images at different depth intervals, b) Mean subtraction method, c) Step-down exponential filtering.

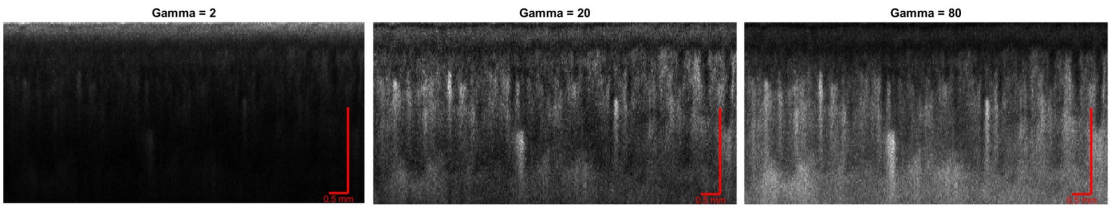

Figure 4.3: Step-down exponential filtering with different gamma values.

4.1.2 Motion artifact

Skin imaging is strongly affected by motion artifacts. The sources of the movements might be involuntary movement of the subject, cardiac or respiratory activities, tremors of the skin. An hardware method can be adopted by lowering the interscan time but of course this has its limitations. The approach used to attenuate via

software the white lines artifacts consists in the merging of two OCTA dataset of the same skin area but acquired orthogonally.

Without moving the patient, it was easy to get a **second acquisition volume** perfectly perpendicular to the first one by simply exchange the driving voltage input of the pair of galvanometers. In this way the y direction becomes the fast scanning direction and the x direction would be the new slow one. The second volume acquired appears to be flipped in respect to the x direction and rotated of 90 degrees around the z axes clockwise.

Once get both volumes, it is necessary to locate the B-scans suffering from this artifact in either. To do so, a first **threshold method** was applied. If the mean intensity of a B-scan overcome the threshold, it is considered corrupted. The threshold is the summed flow median through the B-scans added to twice the standard deviation of it. When local vascularity increases or decreases to a level beyond that of normal tissue, e.g. angiogenesis during wound healing, adopting a simple threshold technique could deliver inaccurate results by either mistakenly regarding a normal region as an artifact or by erroneously taking an artifact as true data [16].

For this reason, a **peak detection technique** was chosen. The same mean profile over all the B-scans were analyzed. The motion affected ones are related to the peaks found over the profile. The peaks were detected under the only condition that they have a relative importance of at least twice the standard deviation of the profile data.

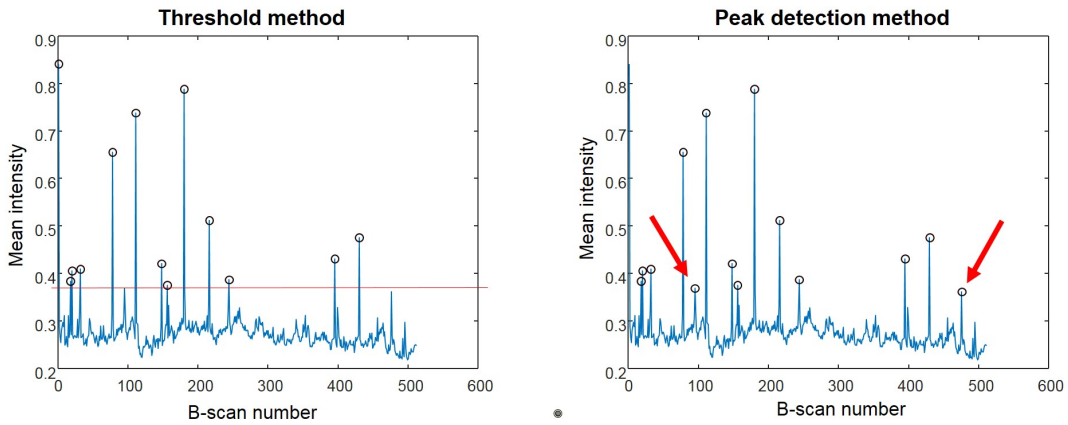

Figure 4.4: Detection of the B-scans affected by motion artifact with threshold and peak detection methods.

Fig. 4.4 highlights with the red line the threshold automatically taken by the algorithm and with the red arrows the peaks that were correctly detected by the second method and instead ignored by the first one. The B-scans thus detected are zeroed.

The **merging** of the two tomograms is done by replacing the zeroed B-scans of a volume with the B-scans of the other volume flipped and rotated. I am aware that a more sophisticated merging technique would include a co-registration of the two volumes and an interpolation. At the crossings of white lines from two orthogonal scans, valid data is not available [17]. The gaps in data can be avoided with high probability by registering additional scans in either or both scanning directions [17].

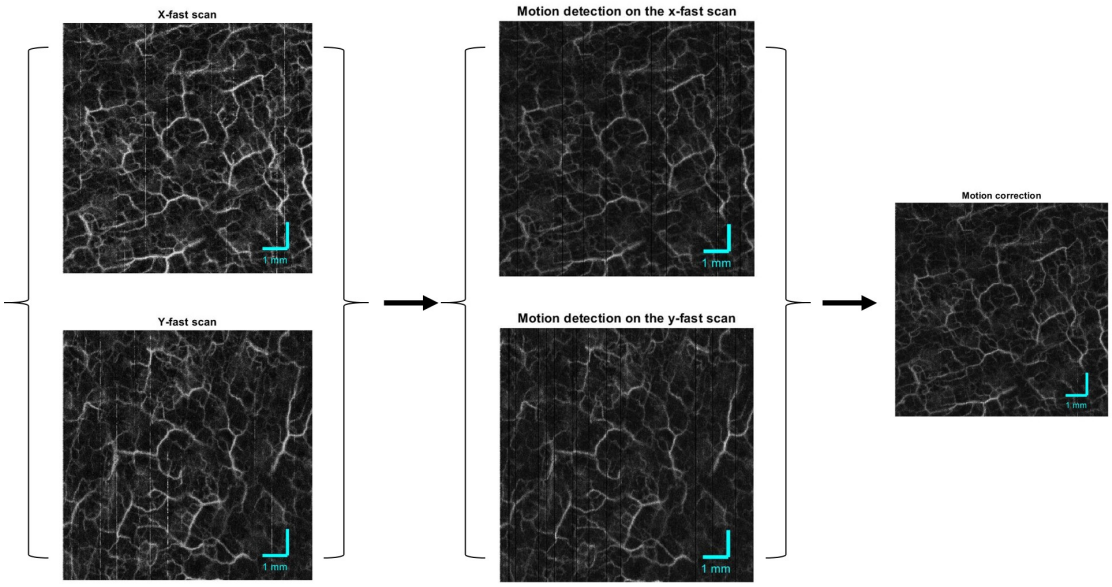

Figure 4.5: Motion artifact attenuation process.

If the double acquisition didn't take place in the imaging session, a simple reduction of the intensity of the affected B-scans is performed. This doesn't allow to get back the information of the affected B-scans but it will at least permit a better visualization to the remaining part of the tomogram.

In any case the performance of the motion artifact attenuation are not highly satisfactory and angiograms that are extremely affected by motion artifacts were discarded.

4.2 Image enhancement

The quality of the corrected OCTA tomograms was further enhanced with the following image processing techniques. The images presented in this section are taken from an acquisition of a seborrheic keratosis lesion on the lower part of the leg and Fig. 4.5 illustrates its raw features.

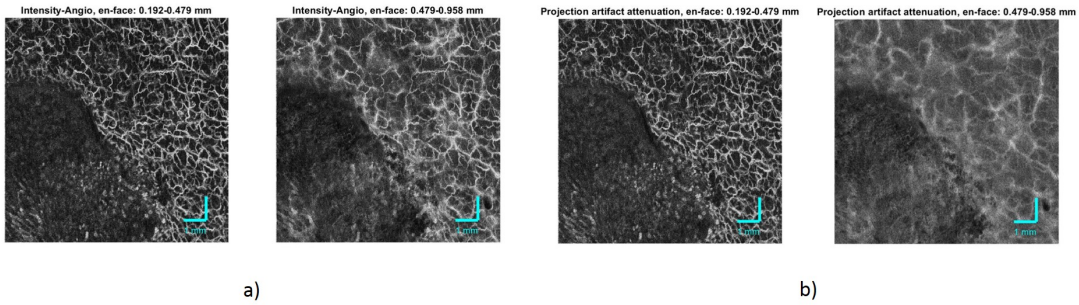

Figure 4.6: Seborrheic keratosis dataset. Intensity OCTA en-face images at two different depth intervals before (a)) and after (b)) projection artifact attenuation.

4.2.1 Smoothing filter

The imaging filters obtain an output image by applying a linear shift invariant (LSI) system to the input image. In other words the input image is convoluted to the impulse response of the LSI system. This operation can be interpreted as a multiplication with a kernel centered on the analyzed pixel of the image and a sum of the resulting values; then the kernel is shifted through the pixels until the operation is done over the entire image. Since we are dealing with tomograms and not with 2D images, the working principle remains the same but the kernel has 3 dimensions and its size chosen for the filtering was [3 3 3].

To reduce the noise superimposed to the dataset and prepare the OCTA tomogram for the next steps of the segmentation algorithm, low pass filters, also called smoothing filters, are adopted. The one adopted in this thesis work is a non linear smoothing filter: a **median filter**. It is not a convolutional filter but it still operates locally. At the pixel located at the center of the kernel it is assigned the median value of the pixels in the neighbourhood. To do so the Matlab function *medfilter3* was applied to the OCTA dataset.

The median filter is preferred in respect to a mean or gaussian one because instead of just smoothing the image, it removes the *salt and pepper* noise that strongly affects our datasets. With this type of filter the histogram of the output

tomogram remains unchanged unless the peaks at the extremes of it, that correspond to the white and black colours. After the median filtering we obtain a tomogram with an higher SNR and with the vessels contour preserved.

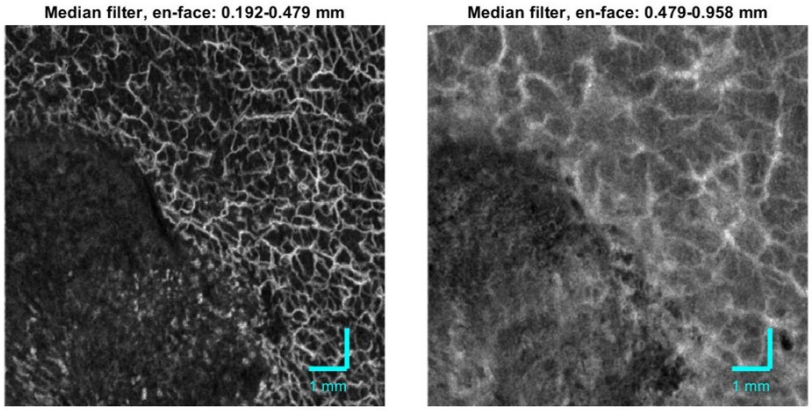

Figure 4.7: Median filter

4.2.2 Contrast enhancement

Contrast is one of the basic parameters for assessing the diagnostic quality of an image. It reports how an object distinguishes from the background. Because the images obtained till this step of the algorithm are characterized by a low contrast, an enhancement of it was performed.

The goal is to increase the luminosity of the brighter pixels and lower the luminosity of the darker ones. The luminosity level that allows to declare a certain pixel as bright or dark is the mean intensity value over all the dataset, also called **luminance**. The value of the pixels that overcome the luminance is increased proportionally to its deviation from the luminance. The same procedure is carried out on the pixels below the luminance, lowering their value.

The appropriate percentage of the increase or decrease of intensity values is found to be the +40% of their deviation from the luminance.

4.2.3 Vesselness enhancement

Before segmenting the vessels it is important to enhance their correct shape and geometry. **Frangi filter** is a way to see vascular structure in the image and better

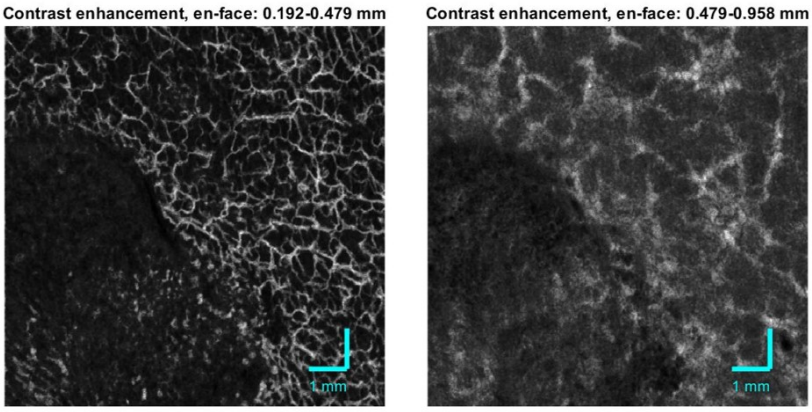

Figure 4.8: Contrast enhancement.

distinguish it from the other structure (residual artifacts and background noise). The filter is implemented with an already existing algorithm in Matlab [18].

The Frangi filter takes advantage of the second order local structure of the 3D image, that is the second-order partial derivative of the tomogram, also called **Hessian matrix**. The eigenvalues, λ_1, λ_2 and λ_3, extracted from the Hessian matrix highlight the information of the 3 orthogonal directions of each voxel. The vesselness function that gives an indication of how likely it is that the structure analyzed is a tubular structure is:

$$V_o(s) = \begin{cases} 0 & if \lambda_2 > 0 or \lambda_3 > 0 \\ (1 - e^{-\frac{R_a^2}{2\alpha^2}}) e^{-\frac{R_b^2}{2\beta^2}} (1 - e^{-\frac{S^2}{2c^2}}) & \end{cases} \tag{4.3}$$

where α, β and c are thresholds which control the sensitivity of the line filter to the measures R_a, R_b and S [19]. R_a and R_b are functions of the eigenvalues and they determines if it is a line or a plane-like structure and the deviation from a blob shape, respectively. S defines the different scales of the vessels that we are able to find.

As suggested in [19] the values of α, β are 0.5, 0.5. The S parameter is more critical, because small values could create false small vessels in the image, whereas high values doesn't allow the detection of the true small vessels. A compromise has been found and two different ranges are provided to the algorithm for the shallower layers (with smaller vessels) and for the deeper layers (with larger vessels): [1 4] and [4 8].

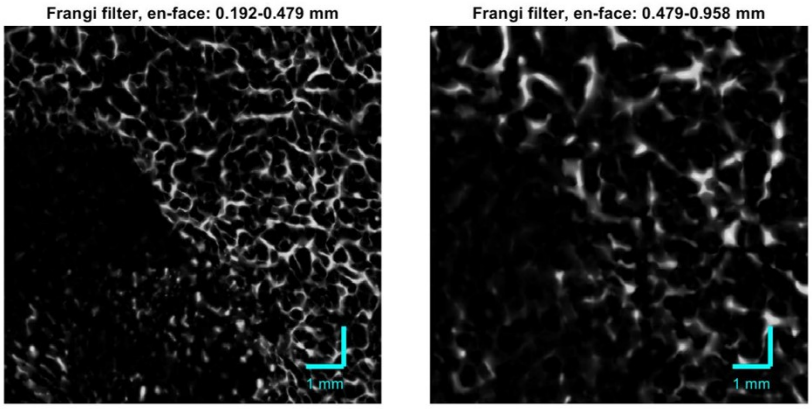

Figure 4.9: Frangi filter.

4.3 Segmentation

The next step is the segmentation of the vascular network through the entire tomogram. This will be fundamental for the extraction of the skeleton later on. Various techniques can be setup but the **global thresholding** method is the one the best fits the vascular images.

It is an easy technique that utilizes the luminosity histogram of the OCTA dataset. The global thresholding works properly in our case because all the tomograms have a bimodal intensity histogram: one mode represent the pixels belonging to the background and the other one the pixels belonging to the vessels. The technique consist in finding a proper threshold on the histogram that separates better the two intensity zones. The pixels of the tomogram which value overcome the threshold will be assigned to the white colour, the ones under-threshold are considered black. The result is a binary volume where white vessels lay over a black background.

The advantages of the technique are:

- if the intensity histogram is bimodal (as in all our cases) the system is computationally easy and immediate,
- its success is independent of the shape and quantity of the objects; it is a pretty versatile technique.

On the other hand, the threshold choice is critical. If it is too high, the vessels

are thinner and probably some flow information is lost; if it is too low, an over-segmentation takes place and more vessels might be represented unified creating false flow.

The search of the **threshold** was performed in three manners:

- by taking the 80% of the quantile of the intensity values of each en-face layer
- by implementing the Otsu method with the Matlab function *otsuthresh*. It assumes that the histogram is the overlapping of two gaussian. The Otsu method finds the threshold that minimizes the gaussian tails.
- by applying a local adaptive thresholding over the tomogram. The Matlab function *adaptthresh* fulfills the purpose.

A comparison between the results of the three threshold finding methods is shown in Fig. 4.10. While the local adaptive threshold over-segments the vessels creating false blood flow information, the quantile method develops disconnection between blood vessels. The Otsu method, indeed, seems to segment more accurately the angiograms.

Once obtained the binary mask, a series of operations can be made in order to extract more precise and clean morphologies from the 3D volumes:

- **Closing**
  A morphological closing is an operation composed by a dilation followed by an erosion. Both of them use the same structuring element that is a binary mask where the ones determine an N-connected space of a certain shape, in this case a sphere of radius 2. The structuring element passes over the data matrix and a binary convolution is carried out. While the dilation replaces the pixel under consideration with the maximum element found in the N-connected space, the erosion replaces it with the minimum. The combination of the two operations in this order removes the background in favor of objects and it is widely used for hole filling and gap filling in disconnected vessels.
- **Cleaning**
  The cleaning process removes isolated voxels, therefore not belonging to any vessel but coming from the background noise. An isolated voxel is an individual pixel set to 1, surrounded by 26-connected voxels set to 0.

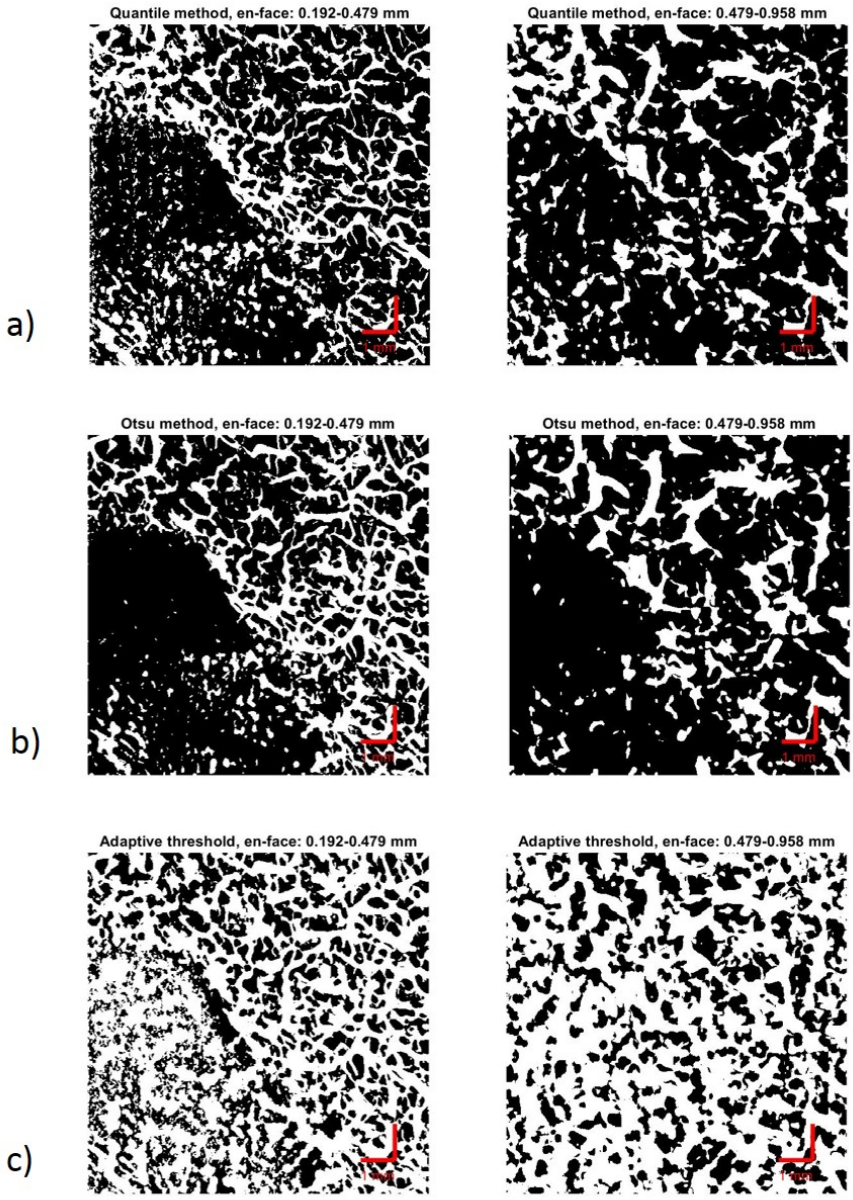

Figure 4.10: Segmentation results from the three different methods presented.

4.4 Skeletonization

To reduce the vascular segmentation to the minimum representation that maintains the vessels morphology we use skeletonization. Skeletonize means to thin the information of the vessels in order to capture the essential figures of the investigated

image or volume. The main problem is that between the skeletonized lines, some disconnections might show up. Moreover noisy pixels in the input volume can portray skeleton lines that do not actually represent the morphology of the blood vessels.

In order to compensate these problems I propose a comparison between three skeleton implementation. Two of them are based on two different Matlab coding of the same algortihm model presented in [20]: *Skeleton3D* and *bwskel*. The third one is a combination of the Matlab function bwskel and the so called *distance transform*.

Skeleton3D vs *bwskel*

[20] adopted a medial axis technique to extract the skeleton; this is suitable for the blood vessels morphology. The two functions, *Skeleton3D* and *bwskel*, are based on the topology of the dataset and as input, they need the binary volume found in the previous section. Their outputs consist in a set of connected points obtained after deleting repeatedly the boarding points of the objects, until the number of connected vessels and Euler characteristic are no more preserved. The Euler characteristic depends on the number of connected objects, holes and cavities of the binary mask. A point in the matrix is considered on the border of the vessel if it has at least one zero pixel in its 26-connected neighbourhood.

Once located the border points a decision tree helps to define which of them can be deleted or not. After each removal step, an update of the border pixels is done and so on. A border pixel is considered in the deletion process until the Euler characteristic doesn't change.

The two resulting skeletonization are similar but I noticed that *bwskel* avoid more vessels disconnections.

Distance transform and *bwskel*

The topology approach can be preceded by a geometric one. The term **distance transform** indicates a matrix of the same dimension of the original dataset and where each pixel establishes how much that voxel is distant from the nearest voxel of the opposite value. In other words it defines the minimum distance from the border of the object itself. High values in the distance transform indicates inner voxels of the vessel, lower values indicates superficial voxels. The points that have a null value in the distance transform are the border points.

A simple way to thin the vessels is to delete the points that have a distance transform value lower than a certain threshold. We can immediately see the main disadvantage of this technique: choosing the right threshold. With a low threshold, disconnections along the vessels lines will surely occur; with an high threshold, the algorithm is not very effective. Again the function *bwskel* applied to the distance transform matrix encourage the skeletonization.

With a qualitative analysis over the resulting skeleton images, the Matlab function *bwskel* seems to be the preferred technique.

A **depth color coding** was implemented by assigning a different color to each en-face layer of the skeletonized tomogram. Fig. 4.11 depicts the maximum intensity projections of the color coded skeletons of a seborrheic keratosis (a)), a wound (b)) and a cherry angioma (c)) dataset.

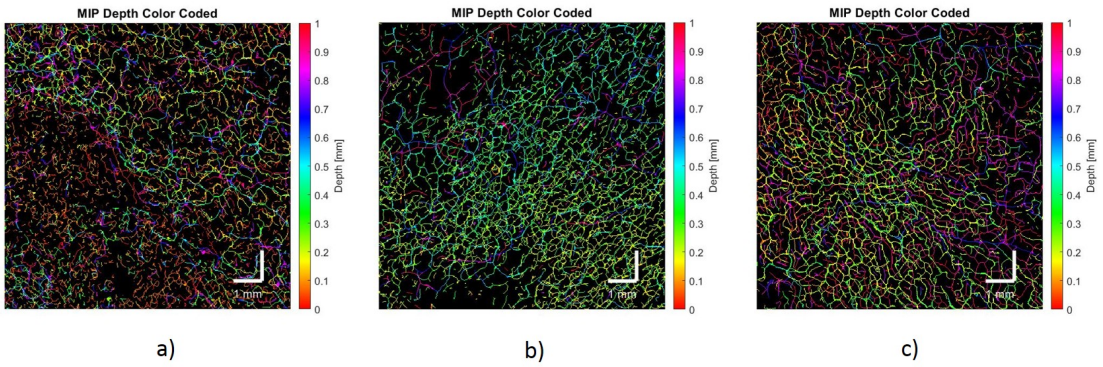

Figure 4.11: MIP depth color coded of a seborrheic keratosis (a)), a wound (b)) and a cherry angioma (c)) skeletonized dataset.

Chapter 5

Parameters extraction

An image has a very complex information content, so summarizing an image in numbers is very complicated. Some characteristics are visible to the human eye but it is necessary to translate that information in a quantitative way; other characteristics are not even visible and only an algorithm can evaluate those. To numerically characterize a vascular network it is useful to extract features and numerical descriptors from the skeleton that represents it and from the OCTA matrix itself.

In the third chapter we already discuss what distinguishes a diseased vascular network from an healthy one. Only one descriptor is not sufficient; this is why more parameters are extracted from the same region and evaluated together. Basically the relevant features are the morphology of the vessels, the grade of toruosity of the network and the texture of the images. The approach requires an analysis of **12 different parameters** from different **regions of interest** (ROIs) of the OCTA post processed volume. Unfortunately only few of them will turn out to be useful for the datasets available for this thesis work.

The entire 3D volume is divided in ROIs which dimensions are 2.5 mm x 2.5 mm x 0.3 mm [21]. The adjacent ROIs are overlapped for a 30% of each dimension in every direction, x, y and z. The overlap areas are filled with the mean value of the parameters calculated in each of the overlapping ROIs. This allows a smoother evaluation of the parameters in different regions of the volume.

Two more clarifications. The morphological and tortuosity parameters chosen are all extracted from the skeletonized volume, unless the mean radius that requires also the segmented vascular matrix; while the texture features are extracted from the OCTA volumes directly. Secondly, the algorithm used for this purpose took inspiration from [22] and [23]. Let's analyse briefly which and how each parameter

was extracted.

5.1 Morphological parameters

5.1.1 Number of vascular trees and number of branchpoints

First of all the singular vascular paths needs to be found. To do so the branchpoints and endpoints are searched thanks to the Matlab function *bwmorph3*. Nevertheless a further check over the detected points is made.

- The Matlab function declares a point as a **branchpoint** if it has at least three white pixels in its 26-connected neighbourhood. But in order to check if those three pixels belong to three different vessels, an additional inspection is made on their 26 neighbours. If the white pixels in the neighborhood of each of those three pixels doesn't belong to the neighbourhood of each other, the original point is effectively a branchpoint. Otherwise it will be removed from the branchpoints list.
- The Matlab function declares a point as an **endpoint** if it has maximum one white pixel in its 26-connected neighbourhood. But if two white pixels belonging to the same vessel appear in the 26-connected set, there will be an underestimation of the endpoints. Hence if the two white pixels are adjacent, the original point is considered an endpoint anyway.

The next step is the execution of a pre-implemented **breadth-first search (BFS)** based algorithm in order to label each vessel path. The algorithm is based on viewing a raster image not as a pixel matrix, but as a graph, whose vertices represent pixels, and whose edges represent neighborhood between pixels [14]. With BFS the pixels to be analyzed are stored in a queue and as a consequence the memory is used in an efficient way. The main steps are:

- search of the connected object with the Matlab function *bwconncomp*. The objects with area smaller than 20 pixels are not taken into account
- for each connected object search of the longest path with the Matlab function *bwdistgedesic*. Insertion of it in a zero matrix with the same dimension of the skeleton one and removal of it from the skeleton matrix.
- analysis of the branches starting from the endpoints found previously. Each branch with an area greater than 10 pixels is searched, removed from the original matrix and put in the new matrix.

As a result the number of independent vascular trees (**VT**) and the number of branchpoints (**NB**) in each ROI is obtained.

5.1.2 Vascular density

The vascular density (**VD**) is an important parameter to distinguish a diseased area from an healthy one. It is independent from the single vascular trees, because it is defined as how many pixels in the ROI belong to the skeleton in respect to the total area of the ROI.

$$VD = \frac{number\ of\ skeleton\ pixels}{number\ of\ ROI\ pixels} \tag{5.1}$$

5.1.3 Mean radius

The extraction of the vessels mean radius (**MR**) is quite critical, not so much for the complexity of the algorithm, but for the accuracy of the results. The algorithm uses both the skeleton and the vessel segmented ROI. The main steps are the following:

- Application of the function *bwperim* to extract the perimeter of the vessels.
- Calculation of the geodesic distance between each point of the perimeter and each point of the skeleton with the function *bwgeodesic*.

An issue hinders the success of the algorithm. We know that the conversion from pixel to mm is different in the lateral and in the axial direction. For the lateral direction 1 pixel correspond to 19,5μm, whereas in the axial direction 1 pixel is equal to 9.6μm. Until we are not able to know in which direction each distance is measured, the conversion from pixel to mm cannot be accurate.

5.2 Tortuosity parameters

The tortuosity parameters are calculated for each vessel path of each skeletonized ROI.

5.2.1 Distance metric

Measuring the distance metric is the easiest way to estimate the vessel tortuosity. It expresses how the vessel line deviates from the straight line between its two extremes. The distance metric (**DM**) is defined by the formula:

$$DM = \frac{\sum_{k=2}^{N} \sqrt{(P_x(k) - P_x(k-1))^2 + (P_y(k) - P_y(k-1))^2 + (P_z(k) - P_z(k-1))^2}}{\sqrt{(P_x(N) - P_x(1))^2 + (P_y(N) - P_y(1))^2 + (P_z(N) - P_z(1))^2}}, \tag{5.2}$$

where N is the length of the path taken into account and P_x, P_y and P_z are the x,y and z coordinates of the k-th point of the path into the ROI matrix.

Expressing the formula into words, DM is the ratio between the actual vessel length and the linear distance between its endpoints. The main disadvantage of this tortuosity measure is that it is able to figure out how far the path of the vessel deviates from the straight line between the endpoints, but not in what way.

5.2.2 Inflection count metric

The inflection count metric (**ICM**) is an extension of the DM. It allows to differentiate two different vessels path with the same DM value by counting their inflection points.

A point of the line in the 3D space is called **inflection point** if at that location the curve changes concavity. In particular, the Normal and Binormal axes of the Frenet frame change orientation by close to 180° as the frame passes through an inflection point [24]. Essentially the Frenet frame is a orthonoraml basis in the 3D Euclidean space, combination of the tangent **T**, normal **N** and binormal **B** unit vector. The derivation of the Frenet frame is shown in Fig. 5.1 and explained here:

- Vectors T1 and T2 connects the adjacent points P(k) and P(k-1) and P(k+1) and P(k), respectively.
- V is the vector between P(k+1) and P(k-1).
- The vector A is the difference between the vectors T2 and T1.
- The tangent vector of the Frenet frame is obtained by normalizing the vector V.
- The normal unit vector N is obtained by the normalization of the cross product of V and A further cross multiplied by V. N is coplanar with the vectors A and V and perpendicular to T.
- Lastly the binormal unit vector B is the cross product of T and N. It is perpendicular to the plane individuated by the other two Frenet frame vectors.

Each point of the skeleton has its own Frenet frame. The inflection points count focuses on the direction of the normal vector. Since the A vector is null at the inflection point, the N vector there is not defined. In fact the point immediately before and immediately after the inflection point have almost opposite orientations of the N vector. Another way to explain it is by the common knowledge that the normal vector always points at the center of the osculating circle; whenever the

concavity of the curve change sign, the normal vector rotates of almost 180 degrees.

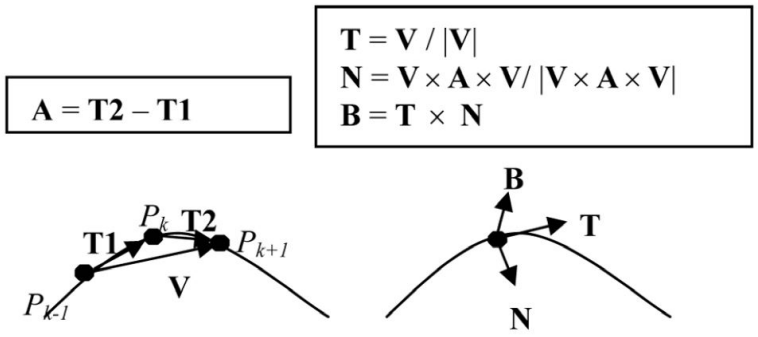

Figure 5.1: Derivation of the Frenet frame. [24]

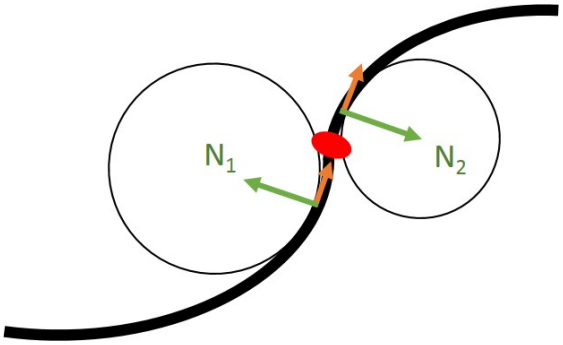

Figure 5.2: Inflection point (red dot) and the opposite directions of the N vectors before and after it (green arrows).

Calling ΔN the difference between to consecutive normal vectors N, this will have its maximum values right in the inflection point. In mathematical words, the inflection points are located where the function $\Delta N \cdot \Delta N$ have its maxima. We are not interested in the location of this inflection points but only in their quantity in each vessel path. This is the reason why the ICM is calculated in the following way:

$$ICM = DM \cdot (N_{inf} + 1), \tag{5.3}$$

where N_{inf} is the number of inflection points obtained as the number of maxima in the function $\Delta N \cdot \Delta N$. Just a note: the addition of 1 to the value of N_{inf} is introduced to avoid a null value of ICM in case of no inflection points found.

The advantage of this technique consists in the quantification of the vascular tortuosity with a higher sensitivity; however there is still a limitation in discerning

coils. The coils increase of course the tortuosity measure of the vascular network, but their structures don't change concavity so they are not detected from the inflection counts metric algorithm. To solve the issue, sum of angles metric (SOAM) has been introduced.

5.2.3 Sum of angles metric

As the name suggest, this parameter describe the total curvature of the skeleton paths. Three types of angle measures are taken into account, afterwards combined together:

- The **in-plane angle**, IP
  This is a measure of the angle between the two vectors T1 and T2.

$$IP = \arccos\left(\frac{T_1}{\|T_1\|} \cdot \frac{T_2}{\|T_2\|}\right). \tag{5.4}$$

  IP gives an estimation of how much the three points (P(k-1), P(k) and P(k+1)) are collinear. The more the value of the angle tends to 0, the more the points are collinear. The maximum value obtainable is π.

- The **torsional angle**, TP
  The torsion at point Pk is represented by the angle between the plane of the current osculating circle, whose surface normal is the normalized cross product of the vectors T1 and T2, and the surface normal of the subsequent osculating plane defined by points P(k), P(k+1), and P(k+2) [24]. By naming T_3 the vector between the points P(k+2) and P(k+1), the TP parameter is calculated as below:

$$TP = \arccos\left(\frac{T_1 \wedge T_2}{\|T_1 \wedge T_2\|} \cdot \frac{T_2 \wedge T_3}{\|T_2 \wedge T_3\|}\right) \tag{5.5}$$

The **total angle of curvature** is:

$$CP = \sqrt{IP^2 + TP^2} \tag{5.6}$$

Finally the **SOAM** parameter is calculated by implementing the formula: [24]

$$SOAM = \frac{\sum_{k=1}^{N-3} CP_k}{\sum_{k=1}^{N-1} \|P_k - P_{k-1}\|}. \tag{5.7}$$

5.3 Texture features

Lastly five parameters are calculated from each ROI extracted from the OCTA tomogram. Those features take into account each pixel belonging to the ROI.

- **Mean**
  A simple mean over all the intensity values is measured.

- **Variance**
  In the same way it has been calculated how much the pixel values differ within the same ROI analyzed with the function *var*.

- **First order entropy**
  The *entropy* Matlab function applies the formula:

$$Entropy = -sum(p. * log_2(p)), \tag{5.8}$$

  on the normalized histogram counts p of the ROI's pixels. The resulting value indicates a measure of randomness of the input dataset.

- **Kurtosis**
  This parameter is a measure of how much the tails of the distribution of the data differ from the tail of a normal distribution. In other words it indicates how much the distribution is flatten or stretched and so how much data are affected by outliers. The Matlab function *kurtosis* was applied to the ROI's values. Distributions that are more outlier-prone distributions results in a higher kurtosis value.

- **Skewness**
  The function *skewness* calculates the homonymous parameter. Its value is related to the asymmetry of the data around the sample mean.

Chapter 6

Results

6.1 Automatic lesion area determination

At this point a heat map is created for each parameter and multiplied by the skeletonized matrix. In Fig. 6.1, 6.3 and 6.5 we can see the maximum intensity projection of the heat maps of each parameter applied over the skeleton for the wound, seborrheic keratosis and cherry angioma datasets respectively.

Each type of lesion has its own type of vascular patterns. The parameters have a difference influence on difference vascular pattern. Indeed, for each type of lesion it is necessary to find the parameter, or the combination of parameters, that best helps distinguish the diseased skin from the healthy one.

For the lesions analyzed in this thesis work, the **vascular density (VD)** parameter and the **variance (VAR)** parameter are the ones that best highlight the lesion area. The other parameters don't show a significant changes in their values within and outside the lesion area.

Those are the steps that lead to the **automatic segmentation** of the skin lesion:

- Computation of the maximum value of the parameter map.
- Determination of a threshold that is the 75% of the maximum value found at the previous step.
- Creation of a binary mask where the pixels of the parameter map which value overcome the threshold are white and the others are black.
- Removal of eventual small areas wrongly segmented; thanks to the function *bwconncomp*, only the white object with the maximum area is preserved.

- Tracing of the region boundaries.

The Fig. 6.2, 6.4 and 6.8 shows the results of the automatic segmentation algorithm for the wound, seborrheic keratosis and cherry angioma datasets respectively. Both the VD and VAR parameters are analyzed.

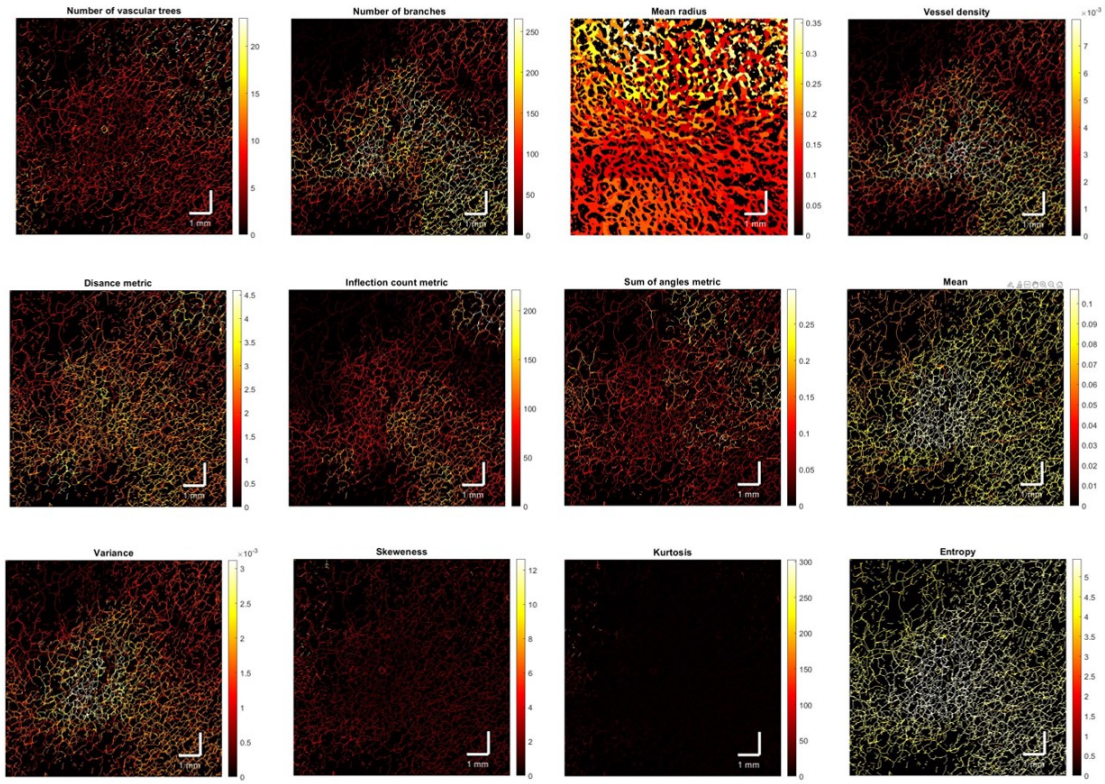

Figure 6.1: Wound dataset. Representation of the parameters values in MIP heat maps.

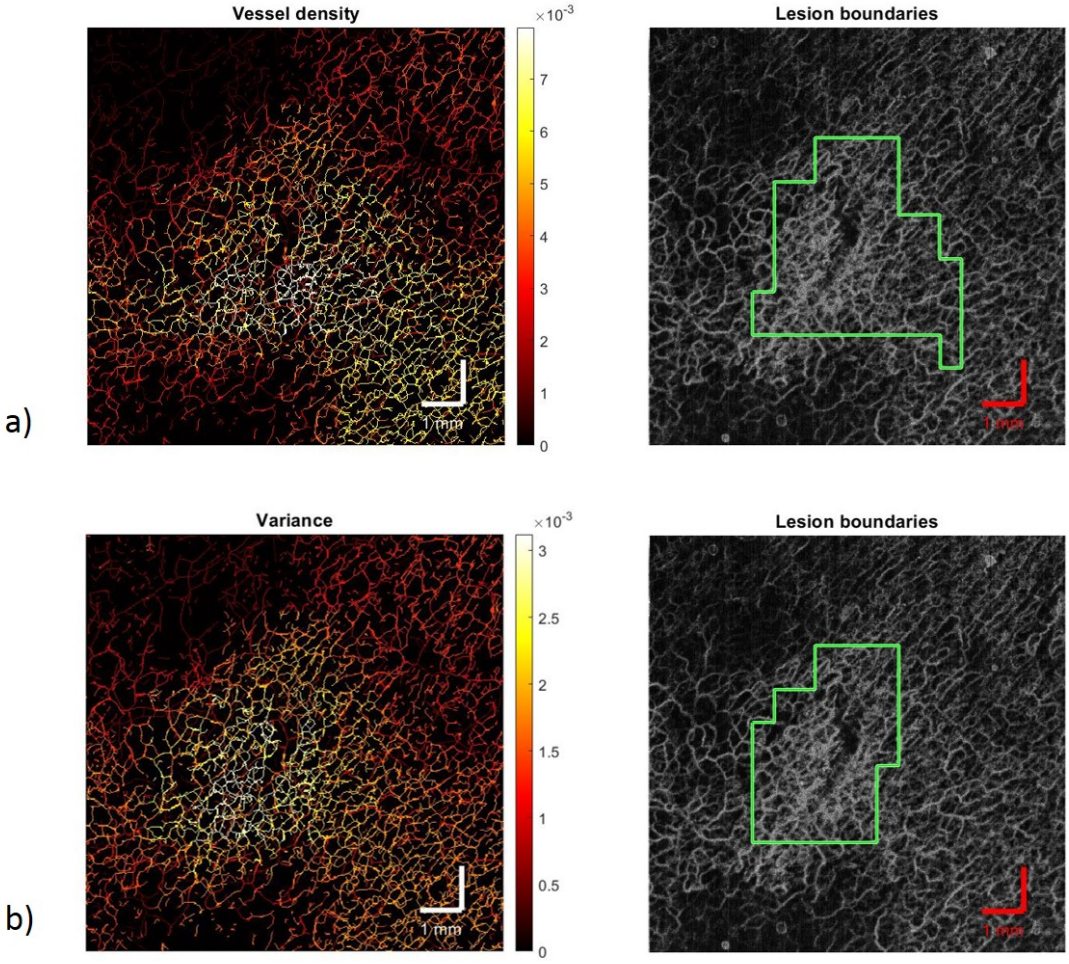

Figure 6.2: Wound dataset. Automatic segmentations performed on the VD heat map (a)) and on the VAR heat map (b)). On the left the heat maps and on the right the corresponding segmentation boundaries visualized over the median intensity projection of the OCTA volume.

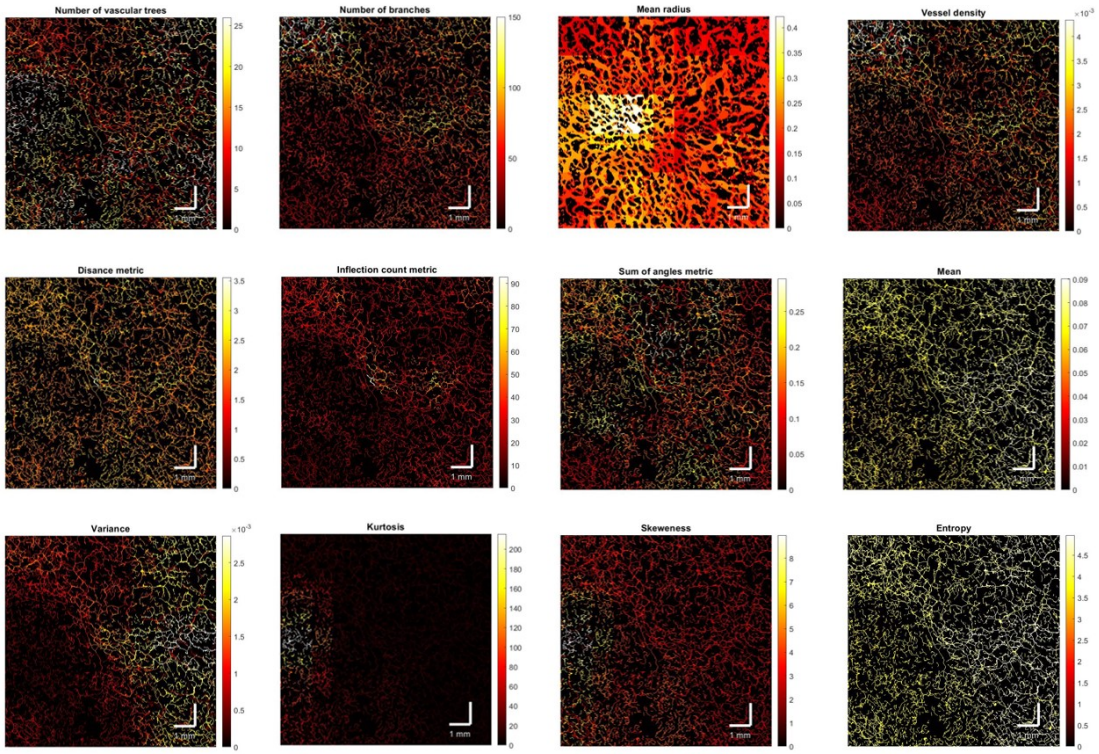

Figure 6.3: Seborrheic keratosis dataset. Representation of the parameters values in MIP heat maps.

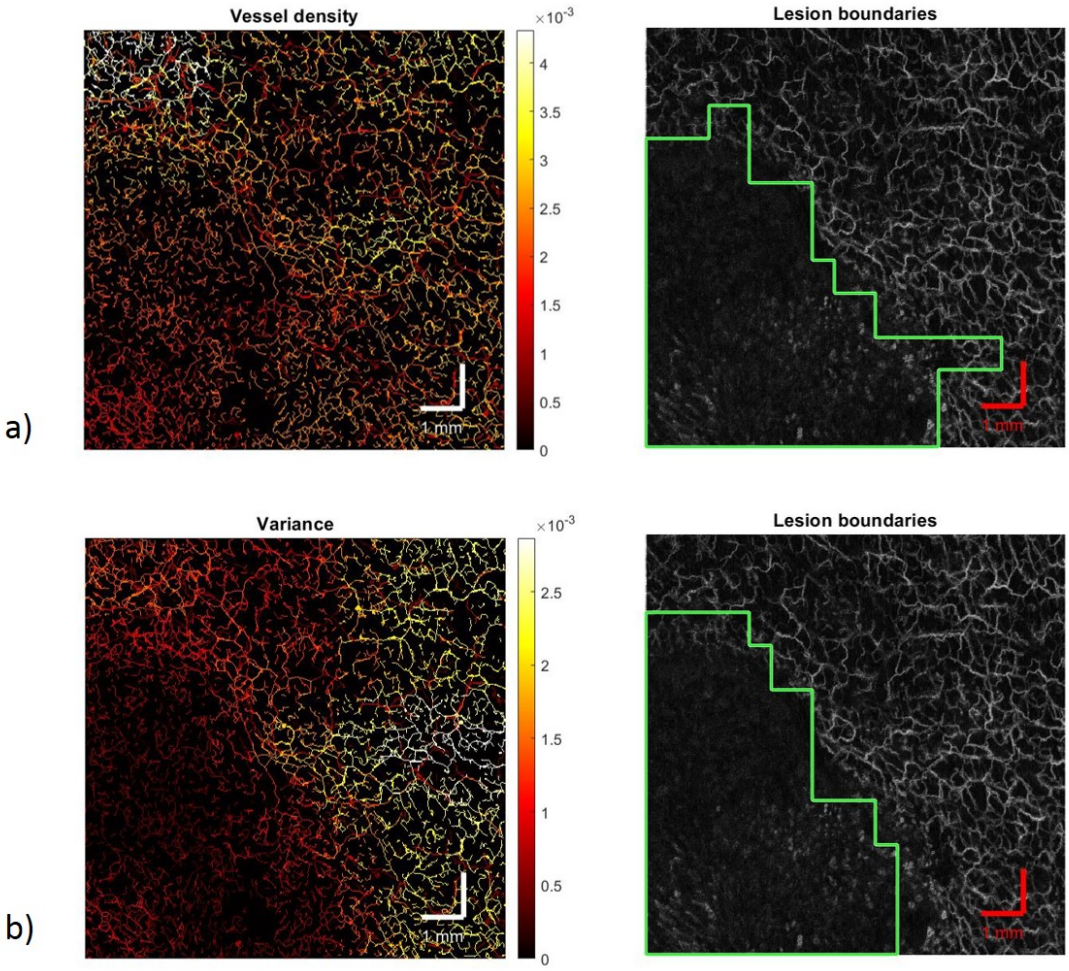

Figure 6.4: Wound dataset. Automatic segmentations performed on the VD heat map (a)) and on the VAR heat map (b)). On the left the heat maps and on the right the corresponding segmentation boundaries visualized over the median intensity projection of the OCTA volume.

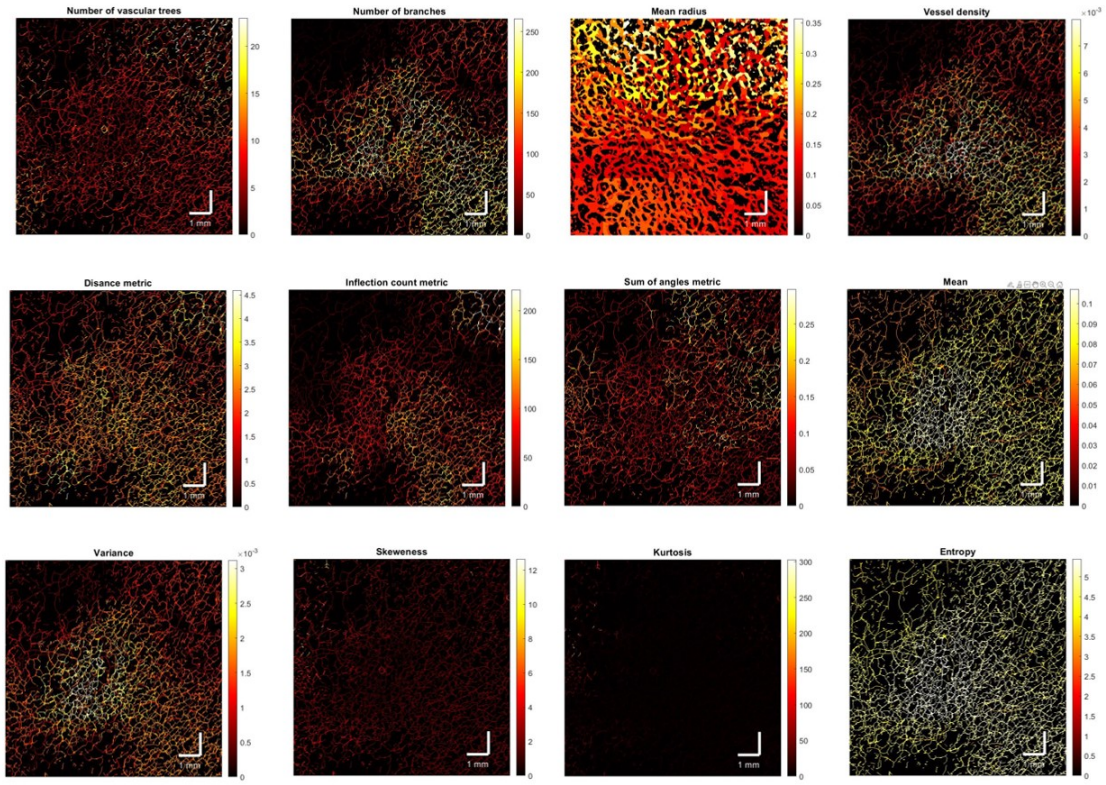

Figure 6.5: Cherry angioma dataset. Representation of the parameters values in MIP heat maps.

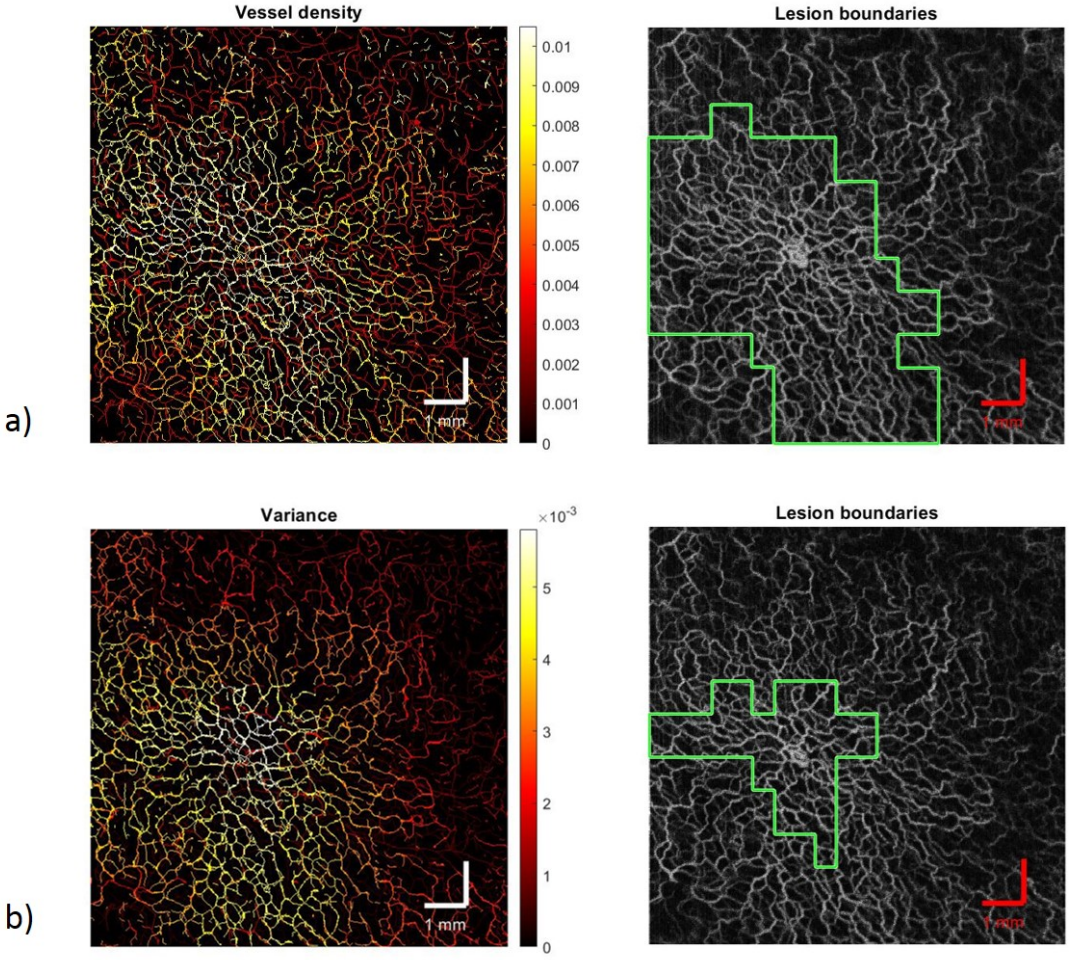

Figure 6.6: Wound dataset. Automatic segmentations performed on the VD heat map (a)) and on the VAR heat map (b)). On the left the heat maps and on the right the corresponding segmentation boundaries visualized over the median intensity projection of the OCTA volume.

6.2 Validation

The system is validated with a discussion over the results obtained with the automatic area segmentation and the manual one performed over the OCTA volume. Moreover a study was carried out to test how the attenuation of the artifacts and the image enhancement of the OCTA volumes have influenced the segmentation output. For this purpose, the parameter extraction and automatic segmentation algorithms were performed on the raw datasets and the results were compared

with the automatic segmentations over the corrected datasets and with the manual segmentations.

In order to highlight divergences and similarities, by comparing the automatic segmentations and the respective manual ones, the following parameters were derived:

- **Difference between the segmented areas dimensions** (diff_area)
- **Dice coefficient** (dice)
  Assuming the manual segmentation as the reference one, the true positives (TP) are the correctly segmented pixels by the automatic algorithm, the false positives (FP) are the pixels that are withe in the automatic segmentation and black in the manual one and the false negatives (FN) are the pixels considered diseased by the manual segmentation but healthy by the automatic one. The Dice coefficient is a similarity measure between two datasets and is implemented by the Matlab function *dice* in this way:

$$dice(manual, automatic) = 2 \cdot \frac{TP}{(2 \cdot TP + FP + FN)}. \tag{6.1}$$

- **Jaccard coefficient** (jaccard)
  The Jaccard coefficient is also a similarity measure and it is performed by the function *jaccard* as follows:

$$jaccard(manual, automatic) = \frac{TP}{(TP + FP + FN)}. \tag{6.2}$$

- **Mean squared error** (err)
  The *immse* function is used for the calculus of the mean squared error of the ROI's values.

In Fig. 6.7 are the comparisons of the three segmentation results over the VD and VAR parameters maps. In the bar diagram of Fig. 6.8 instead the results of the validation parameters listed above.
Some observations:

- The variance parameter seems to be the more accurate in order to differentiate the healthy skin form the diseased skin.
- The automatic segmentation based on the raw data tends to over-segment the lesion area and tends to have an higher divergence from the manual one in respect to the automatic segmentation based on the corrected datset.

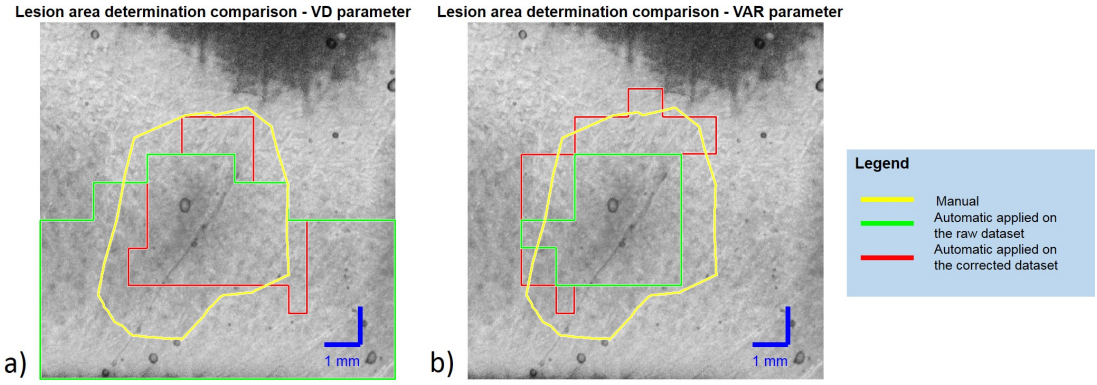

Figure 6.7: Wound dataset. Comparison between the automatic segmentation based on the corrected dataset, the automatic segmentation based on the raw dataset and the manual segmentation performed on the OCTA dataset. The lesion boundaries are visualized over the logarithmic scaled MIP OCT en-face.

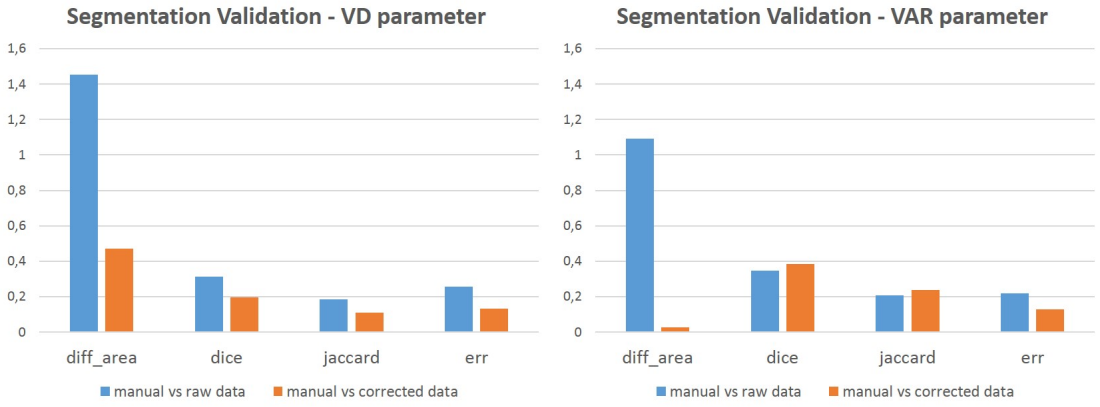

Figure 6.8: Validation parameters.

- The similarity measures highlight a good performance of the algorithm presented in this thesis for the VAR parameter. Whereas for the VD parameter it seems that the automatic segmentation works better with the raw data even if the Fig. 6.7 a) depicts the opposite. This is due to a wrong automatic segmentation of the deeper layers of the skin lesion. In fact the majority of the useful information for the present study are contained in the shallower depth interval while the deeper might undergo to a wrong result.

Unfortunately the available data of skin lesions are not sufficient to validate the considerations made and to make new ones. However a further proof of the methods

exposed in this thesis will continue in the future by imaging new patients.

Moreover in the Fig. 6.9 a numerical comparison of the parameters values between the dataset of the wound and the dataset of a wound already healed is depicted.

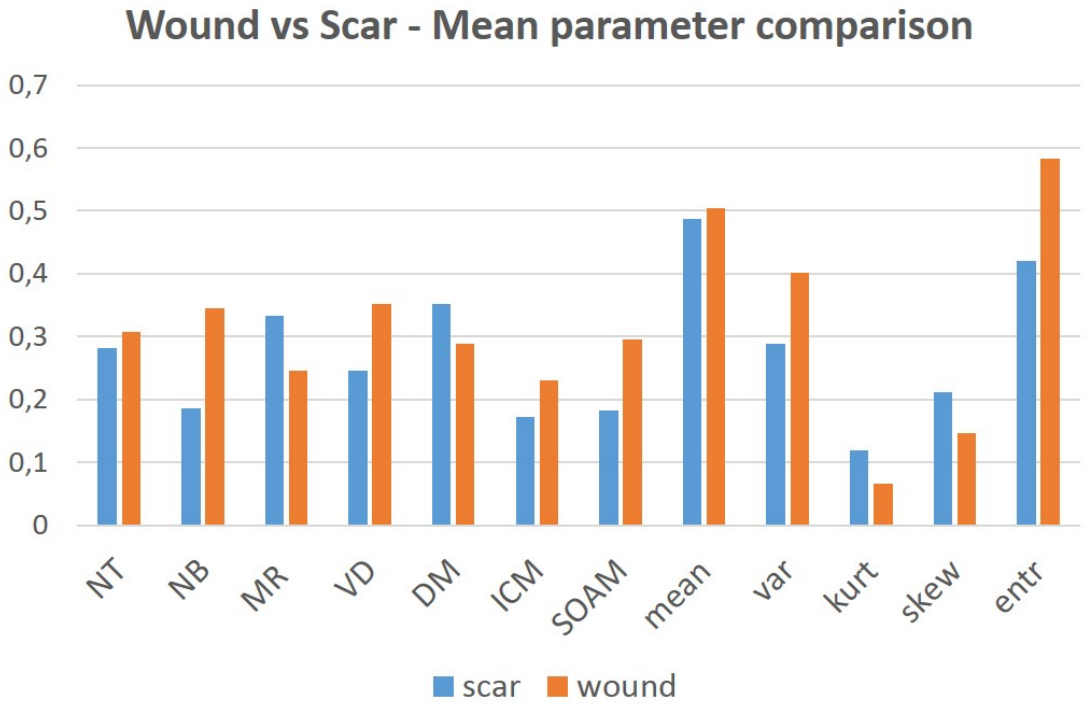

Figure 6.9: Comparison between the mean parameters of the wound dataset and of the scar dataset.

As we expected, the mean VD and VAR values are higher for the wound not healed.

In general the algorithm presented here is able to highlight differences between the healthy vasculature and the blood flow network within the skin lesion. However, the automatic segmentation algorithm still needs to be improved.

Chapter 7

Conclusions and Future Developments

The procedure presented seems to have a wide margin for improvements but at the same time it awaits the initially set goal: a completely non-invasive and automatic way to quantitatively analyze skin lesion through its vascular network.

In general the algorithm presented here is able to highlight differences between the healthy vasculature and the blood flow network within the skin lesion. However, the automatic segmentation algorithm still needs to be improved. Of course to validate the algorithm and improve it other imaging sessions should take place and more data should be analyzed. A proof of concept is on the way of realization.

For sure, since the intelligibility of OCTA images is severely compromised by artifacts, especially by projection artifacts and motion artifacts, their attenuation enabled a better understanding of the angiograms.

Some future developments might be:

- implementation of a neural network on the dataset for a better vessel segmentation.
- application of machine larning or deep learning for the lesion area determination.
- usage of a multimodal imaging technique that combines the OCTA imaging with another technology in order to compensate the limitation of the first one. For example the study [25] integrates photoacustic imaging in order to gain a greater penetration depth.
- design of an OCT system more suitable for patient imaging.

Bibliography

[1] Adolf Fercher, W Drexler, Christoph Hitzenberger, and Theo Lasser. «Optical Coherence Tomography—Principles and Applications». In: *Rep. Prog. Phys* 66 (Feb. 2003). DOI: 10.1088/0034-4885/66/2/204 (cit. on pp. 3–6, 8, 9).

[2] Murtaza Ali and Renuka Parlapalli. «Signal Processing Overview of Optical Coherence Tomography Systems for Medical Imaging». In: *Texas Instrum.* (Jan. 2010) (cit. on p. 7).

[3] W. Drexler, M. Liu, A. Kumar, T. Kamali, A. Unterhuber, and Leitgeb. «Optical coherence tomography today: speed, contrast, and multimodality.» In: *Journal of biomedical optics* 19.7 (2014). DOI: https://doi.org/10.1117/1.JBO.19.7.071412 (cit. on p. 9).

[4] Z. Chen, M. Liu, M. Minneman, L. Ginner, E. Hoover, H. Sattmann, M. Bonesi, W. Drexler, and Leitgeb. «Phase-stable swept source OCT angiography in human skin using an akinetic source.» In: *Biomedical optics express* 7.8 (2016), pp. 3032–3048. DOI: https://doi.org/10.1364/BOE.7.003032 (cit. on pp. 11, 16–18, 20).

[5] Huafeng Ding, Jun Q Lu, William A Wooden, Peter J Kragel, Xin-Hua Hu, and Xin-Hua Hu. «Refractive indices of human skin tissues at eight wavelengths and estimated dispersion relations between 300 and 1600 nm». In: *Physics in medicine and biology* 51.6 (Mar. 2006), pp. 1479–1489. ISSN: 0031-9155. DOI: 10.1088/0031-9155/51/6/008 (cit. on p. 16).

[6] Richard F. Spaide, James G. Fujimoto, Nadia K. Waheed, Srinivas R. Sadda, and Giovanni Staurenghi. «Optical coherence tomography angiography». In: *Progress in Retinal and Eye Research* 64 (2018), pp. 1–55. DOI: https://doi.org/10.1016/j.preteyeres.2017.11.003 (cit. on p. 20).

[7] Jie Wang, Miao Zhang, Thomas S. Hwang, Steven T. Bailey, David Huang, David J. Wilson, and Yali Jia. «Reflectance-based projection-resolved optical coherence tomography angiography». In: *Biomed. Opt. Express* 8.3 (Mar. 2017), pp. 1536–1548. DOI: 10.1364/BOE.8.001536. URL: http://www.osapublishing.org/boe/abstract.cfm?URI=boe-8-3-1536 (cit. on pp. 21, 44).

[8] Lisa Krainz. Center for medical physics and biomedical engineering - Medical Univeristy of Vienna (cit. on p. 23).

[9] SD Guo and L.A. DiPietro. «Factors Affecting Wound Healing». In: *Journal of dental research* 89 (Mar. 2010), pp. 219–29. DOI: 10.1177/0022034509359125 (cit. on p. 31).

[10] Bhutta BS. Greco MJ. *Seborrheic Keratosis*. Feb. 2021. URL: https://www.ncbi.nlm.nih.gov/books/NBK545285/?report=reader#_NBK545285_pubdet_ (cit. on p. 31).

[11] Douglas MS. Higgins JC Maher MH. «Diagnosing Common Benign Skin Tumors.» In: *Am Fam Physician* 92 (Oct. 2015), pp. 601–607. DOI: 26447443 (cit. on p. 32).

[12] Akkurt Z. Ayhan E Ucmak D. «Vascular structures in dermoscopy». In: *An Bras Dermatol.* 90 (July 2015), pp. 545–553. DOI: 10.1590/abd1806-4841.20153452. (cit. on pp. 34, 35).

[13] Marcia G. Tonnesen, Xiaodong Feng, and Richard A.F. Clark. «Angiogenesis in Wound Healing». In: *Journal of Investigative Dermatology Symposium Proceedings* 5.1 (2000), pp. 40–46. ISSN: 1087-0024. DOI: https://doi.org/10.1046/j.1087-0024.2000.00014.x. URL: https://www.sciencedirect.com/science/article/pii/S0022202X15528571 (cit. on p. 36).

[14] Verena Ahlgrimm-Siess, Theresa Cao, Margaret Oliviero, Rainer Hofmann-Wellenhof, Harold S. Rabinovitz, and Alon Scope. «The Vasculature of Nonmelanocytic Skin Tumors in Reflectance Confocal Microscopy, II: Vascular Features of Seborrheic Keratosis». In: *Archives of Dermatology* 146.6 (June 2010), pp. 694–695. ISSN: 0003-987X. DOI: 10.1001/archdermatol.2010.123. URL: https://doi.org/10.1001/archdermatol.2010.123 (cit. on p. 36).

[15] Woo June Choi, Bjorn Paulson, Sungwook Yu, Ruikang Wang, and Jun Ki Kim. «Mean-Subtraction Method for De-shadowing of Tail Artifacts in Cerebral OCTA Images: A Proof of Concept». In: *Materials* 13 (Apr. 2020), p. 2024. DOI: 10.3390/ma13092024 (cit. on p. 46).

[16] Wei Wei, Anthony Deegan, and Ruikang Wang. «Automatic motion correction for in vivo human skin optical coherence tomography angiography through combined rigid and nonrigid registration». In: *Journal of Biomedical Optics* 22 (June 2017), p. 066013. DOI: 10.1117/1.JBO.22.6.066013 (cit. on p. 48).

[17] Stefan B. Ploner et al. «Efficient and high accuracy 3-D OCT angiography motion correction in pathology». In: *Biomed. Opt. Express* 12.1 (Jan. 2021), pp. 125–146. DOI: 10.1364/BOE.411117. URL: http://www.osapublishing.org/boe/abstract.cfm?URI=boe-12-1-125 (cit. on p. 49).

[18] (Cit. on p. 52).

[19] Alejandro F. Frangi, Wiro J. Niessen, Koen L. Vincken, and Max A. Viergever. *Multiscale vessel enhancement filtering*. Ed. by William M. Wells, Alan Colchester, and Scott Delp. Berlin, Heidelberg: Springer Berlin Heidelberg, 1998, pp. 130–137. ISBN: 978-3-540-49563-5 (cit. on p. 52).

[20] T.C. Lee, R.L. Kashyap, and C.N. Chu. «Building Skeleton Models via 3-D Medial Surface Axis Thinning Algorithms». In: *CVGIP: Graphical Models and Image Processing* 56.6 (1994), pp. 462–478. ISSN: 1049-9652. DOI: https://doi.org/10.1006/cgip.1994.1042. URL: https://www.sciencedirect.com/science/article/pii/S104996528471042X (cit. on p. 56).

[21] Kristen Meiburger et al. «Automatic Skin Lesion Area Determination of Basal Cell Carcinoma using OCT Angiography and a Skeletonization Approach: Preliminary Results». In: *Journal of Biophotonics* 12 (May 2019), e201900131. DOI: 10.1002/jbio.201900131 (cit. on p. 58).

[22] K M Meiburger, S Y Nam, E Chung, L J Suggs, S Y Emelianov, and F Molinari. «Skeletonization algorithm-based blood vessel quantification usingin vivo3D photoacoustic imaging». In: *Physics in Medicine and Biology* 61.22 (Oct. 2016), pp. 7994–8009. DOI: 10.1088/0031-9155/61/22/7994. URL: https://doi.org/10.1088/0031-9155/61/22/7994 (cit. on p. 58).

[23] Roberta Bruschetta. «A skeletonization approach for the evaluation of vascular complexity using in-vitro phantoms and 3D LED-based photoacoustic images». Master Degree Thesis. Politecnico di Torino, 2019 (cit. on p. 58).

[24] Elizabeth Bullitt, Guido Gerig, Stephen Pizer, Weili Lin, and Stephen Aylward. «Measuring Tortuosity of the Intracerebral Vasculature From MRA Images». In: *IEEE transactions on medical imaging* 22 (Oct. 2003), pp. 1163–71. DOI: 10.1109/TMI.2003.816964 (cit. on pp. 61–63).

[25] Mengyang Liu et al. «Combined multi-modal photoacoustic tomography, optical coherence tomography (OCT) and OCT angiography system with an articulated probe for in vivo human skin structure and vasculature imaging». In: *Biomed. Opt. Express* 7.9 (Sept. 2016), pp. 3390–3402 (cit. on p. 75).